Correlation Spectroscopy with Multiqubit-Enhanced Phase Estimation

H. Hainzer,[1,2] D. Kiesenhofer,[1,2] T. Ollikainen,[1] M. Bock,[1,2] F. Kranzl,[1,2] M. K. Joshi,[1] G. Yoeli,[3] R. Blatt,[1,2] T. Gefen,[4,*] and C. F. Roos[1,2,†]

[1]*Institut für Quantenoptik und Quanteninformation, Österreichische Akademie der Wissenschaften, Technikerstraße 21a, 6020 Innsbruck, Austria*
[2]*Institut für Experimentalphysik, Universität Innsbruck, Technikerstraße 25, 6020 Innsbruck, Austria*
[3]*Racah Institute of Physics, The Hebrew University of Jerusalem, Givat Ram, Jerusalem 91904, Israel*
[4]*Institute for Quantum Information and Matter, Caltech, Pasadena, California, USA*

(Received 18 February 2023; revised 19 December 2023; accepted 8 February 2024; published 29 February 2024)

Ramsey interferometry is a widely used tool for precisely measuring transition frequencies between two energy levels of a quantum system, with applications in time keeping, precision spectroscopy, quantum optics, and quantum information. Often, the coherence time of the quantum system surpasses the one of the oscillator probing the system, thereby limiting the interrogation time and associated spectral resolution. Correlation spectroscopy overcomes this limitation by probing two quantum systems with the same noisy oscillator for a measurement of their transition frequency difference; this technique has enabled very precise comparisons of atomic clocks. Here, we extend correlation spectroscopy to the case of multiple quantum systems undergoing strong correlated dephasing. We model Ramsey correlation spectroscopy with N particles as a multiparameter phase estimation problem and demonstrate that multiparticle correlations can assist in reducing the measurement uncertainties even in the absence of entanglement. We derive precision limits and optimal sensing techniques for this problem and compare the performance of probe states and measurement with and without entanglement. Using one- and two-dimensional ion Coulomb crystals with up to 91 qubits, we experimentally demonstrate the advantage of measuring multiparticle correlations for reducing phase uncertainties and apply correlation spectroscopy to measure ion-ion distances, transition frequency shifts, laser-ion detunings, and path-length fluctuations. Our method can be straightforwardly implemented in experimental setups with globally coherent qubit control and qubit-resolved single-shot readout and is, thus, applicable to other physical systems such as neutral atoms in tweezer arrays.

DOI: 10.1103/PhysRevX.14.011033

Subject Areas: Atomic and Molecular Physics, Quantum Information

I. INTRODUCTION

The ability to estimate the phase of a wave is key to practical applications such as time keeping with atomic clocks [1], rotation and acceleration sensing [2], and gravimetry [3] but also to probing fundamental physics [4] and measuring fundamental constants of nature [5]. Sensing techniques such as optical or matter wave interferometry rely on phase comparisons of two light waves or matter waves, respectively. In optical atomic clocks, for instance, the phase of an atomic superposition state is compared to the phase of the laser having created the superposition. In most of these applications, a large number of uncorrelated photons or atoms are probed, giving rise to a measurement uncertainty governed by the standard quantum limit according to which the uncertainty decreases inversely with the square root of the number of particles being probed. If, however, quantum correlations exist between the particles, the scenario becomes much more interesting and complex.

In this context, phase estimation based on quantum measurements constitutes a subfield of quantum metrology, which aims at making sensitive measurements of physical quantities by harnessing quantum resources, in particular, entanglement [6]. To this end, it has been shown that entangled input states can be used to beat the standard quantum limit [7,8] and that entanglement can be a resource for achieving optimal phase sensing over a wider range of phases [9]. However, as entangled states easily decohere under environmental noise, the performance gain of entanglement-enhanced metrology protocols can be jeopardized by decoherence processes [10,11]; the achievable precision

*tgefen@caltech.edu
†christian.roos@uibk.ac.at

bounds depend on whether the noise is Markovian or contains temporal or spatial correlations [12,13].

Furthermore, from a practical point of view, entanglement-generating resources are often not readily available in precision experiments. For this reason, it is of interest to consider quantum metrology protocols using quantum correlations other than entanglement that might be easier to implement for carrying out quantum-enhanced measurements [14]. In this paper, we focus on correlation spectroscopy [15,16], a phase estimation technique for probing the phase difference of qubits subjected to spatially correlated noise, and extend it to networks of N qubits. In the following, we provide our motivation for studying this measurement scenario.

Coherent probing of ultranarrow atomic transitions in combination with outstanding characterization of systematic level shifts has led to the development of optical atomic clocks with unprecedented precision [17]. To verify a clock's performance, its frequency has to be compared with another clock. The uncertainty with which the frequency difference of the clocks can be determined within a given measurement time is usually not limited by the lifetime of the atomic energy levels but rather by the local oscillator's phase noise that sets an upper bound to the useful probe time. This limitation can be overcome by synchronous probing of the two clocks with the same local oscillator and correlating the measurement outcomes. In the case of ensemble-averaged signals, such as in optical lattice clocks where the excitation probability of a large number of atoms is measured [18,19], the correlations are purely classical. If, however, the measurements probe the quantum state of individual atoms, the correlations can become nonclassical, even in the absence of any entanglement [20].

It is in this context that correlation spectroscopy [15,16] has been developed, a technique for measuring transition frequency differences in the presence of correlated phase noise with probe times that can be significantly longer than the coherence time of each system with respect to the local oscillator [21–25]. It is based on a synchronous standard Ramsey-type interrogation of two or more atoms by the same oscillator: A first $\pi/2$ pulse rotates the Bloch vector into the equatorial plane, where it precesses during the free evolution time with a rate set by the detuning of the oscillator from the atomic transition. The second $\pi/2$ pulse in conjunction with a state detection in the energy eigenbasis enables the measurement of a spin projection in the equatorial plane. However, instead of measuring expectation values of individual atoms, a parity measurement is used to correlate the measurement outcomes of pairs of atoms. By this approach, transition frequency differences can be measured by observing parity oscillations as a function of the duration of the free evolution time. While correlation spectroscopy achieves only a maximum parity oscillation contrast of 0.5 and, therefore, does not achieve the optimum signal-to-noise ratio obtainable by preparing maximally entangled states of the two systems [26–28], it is technically much easier to implement.

The detection of phase shifts in the presence of strong correlated phase noise is a common scenario that appears in a wide variety of sensing platforms. Apart from the example of multiple clocks probed by the same oscillator, spatially correlated noise can result from the spatial proximity of the qubits [29–31], instabilities of the local oscillator probing them [29,32], or the coupling of the qubits to a common bosonic mode [33,34]. A similar scenario appears also in interferometers and optomechanical sensors where a displacement noise of the mirrors and radiation pressure induce a correlated noise on the different output modes [35–37].

In this work, we investigate the parameter phase estimation scenario as sketched in Fig. 1: We consider a set of N qubits, all of which are prepared in states with Bloch vectors in the equatorial plane and subjected to correlated phase noise [Fig. 1(a)]. We want to estimate the angle between the Bloch vectors of a pair of qubits (i, j) by applying a second $\pi/2$ pulse, measuring all qubits in the energy eigenbasis, and correlating the measurement outcomes (± 1) to obtain the correlation $C_{i,j}$ [Fig. 1(b)]. We ask the question whether the measurement uncertainty of one of the correlations, e.g., $C_{1,2}$, obtained from a finite number of experimental repetitions could be reduced by taking into consideration all other pair correlations that are simultaneously recorded instead of analyzing only the measurements of the particular pair, e.g., (1, 2). We analyze this simple model and show that this is indeed the case. We then proceed to estimate the phases using all N-qubit correlations, not only pair correlations, and show that the uncertainty can be even further reduced. This N-qubit correlations analysis is performed by applying maximum-

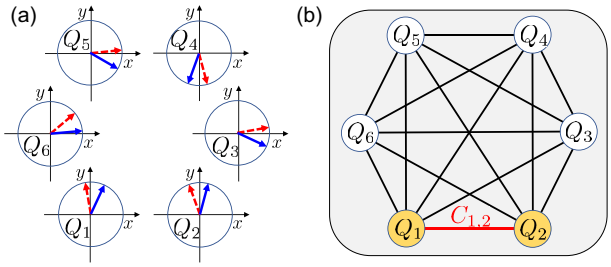

FIG. 1. Measurement scenario. (a) In a network of quantum sensors comprised of qubits Q_i, the qubits are prepared in Bloch states lying in the equatorial plane and subjected to correlated dephasing that randomly rotates all Bloch vectors by the same angle, as indicated by solid and dashed arrows. (b) Correlations $C_{i,j}$ between pairs of qubits (i, j) are measured for an estimation of the angle between the respective Bloch vectors. Is it possible to reduce the measurement uncertainty of $C_{i,j}$ obtained from a finite number of experimental repetitions by taking into account all pair correlations that can be simultaneously measured or even all N-qubit correlations?.

likelihood estimation or Bayesian estimation to the full probability distribution.

In this way, we generalize the notion of correlation spectroscopy to a quantum sensor network of N two-level quantum systems [23,25] and demonstrate, in theory and experiment, an improvement compared to the traditional pair-correlation method. We derive precision bounds when all the $\binom{N}{2}$ pair correlations of the outcomes are used and for the case where all N-qubit correlations are exploited. These methods are implemented in experiments with ion crystals and are used to estimate ion-ion distances and transition frequency shifts. Finally, we propose theoretical schemes for further improvement with entangled measurements and initial states.

The manuscript is structured as follows: In Sec. II, we describe the principle of N-qubit correlation spectroscopy and how the analysis of measured correlations can be used for inferring relative phase shifts between the qubits as well as tracking correlated phase shifts on all qubits in the time domain. Section III demonstrates the implementation of the measurement protocol in one- and two-dimensional ion crystals with up to 91 ions. In Sec. IV, we discuss lower bounds to the measurement uncertainties when analyzing pair correlations or N-qubit correlations and demonstrate that these bounds are nearly saturated in our experiments. We further discuss general quantum precision limits and show that the input states used in our experiments are near optimal in terms of the achievable measurement precision. Section V discusses applications of the method in trapped-ion experiments for the determination of transition frequency differences, ion-ion distances, and tracking of local oscillator noise. In Sec. VI, we discuss the application of our measurement protocol to other experimental platforms.

II. MODEL: N-QUBIT CORRELATION SPECTROSCOPY

We consider a dataset consisting of $m = 1, \ldots, M$ realizations of Ramsey experiments with a free evolution time T, each of which is simultaneously carried out on an ensemble of N qubits [see Fig. 2(a)]. Prior to the second $\pi/2$ pulse, the state of the N qubits during the mth realization is

$$2^{-N/2} \prod_{i=1}^{N} (|0\rangle + e^{i\phi_{im}}|1\rangle), \tag{1}$$

with phases

$$\phi_{im} = \phi_i + \varphi_m, \tag{2}$$

where ϕ_i is a qubit-specific phase and φ_m a random phase that is common to all qubits; i.e., in experiments, ϕ_i appears as a spatially varying phase, whereas φ_m encodes temporal changes. To achieve an unambiguous definition of these phases, we define φ_m to be the phase change between the mth experiment and the first one. The phase φ_m could result from a stochastic process coupling the qubits to an environment inducing correlated dephasing; alternatively, it could be engineered in the experiment, for example, by randomly shifting the phase of the first Ramsey pulse with respect to the second one. Note that we assume temporal variations of the phases φ_m to occur on timescales that are orders of magnitude longer than the time a laser wavefront needs to transit the qubit array. This condition assures that φ_m is indeed the same for all qubits. The qubit-specific phases $\phi_i = (\mathbf{k}_1 - \mathbf{k}_2)\mathbf{r}_i + \Delta_i T$ arise if the qubits have different detunings Δ_i with respect to the local oscillator frequency or if the qubits are excited from different spatial directions for the first and the second $\pi/2$ pulse. Here, $\mathbf{k}_1(\mathbf{k}_2)$ is the k vector of the running wave inducing the first (second) $\pi/2$ pulse and $\mathbf{r}_i$ is the qubit position vector. We assign an outcome $q_{im} = 1$ or -1 to the measurement, depending on whether we observe qubit i in the mth measurement in the state $|0\rangle$ or $|1\rangle$. The probability of observing the outcome q_{im} is given by $p(q_{im}) = \frac{1}{2}(1 + q_{im} \sin \phi_{im})$.

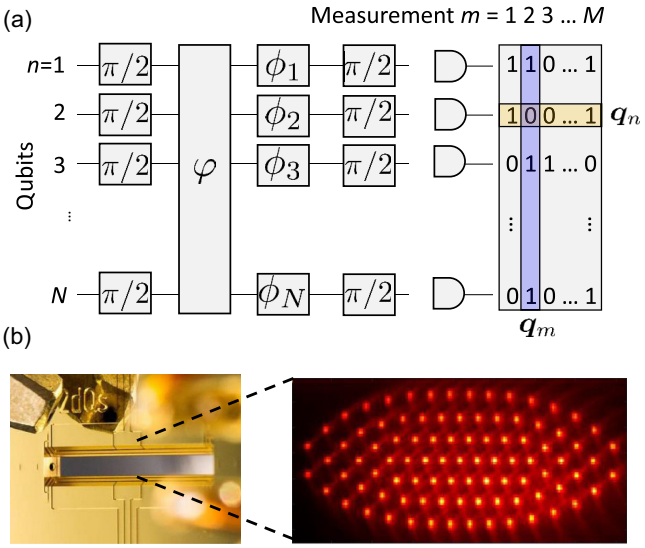

FIG. 2. (a) Measurement protocol: Ramsey experiments are simultaneously carried out on an ensemble of N qubits subject to correlated dephasing, phase shifting all qubits by a random phase φ, and single-qubit phase shifts ϕ_n. The analysis of correlations between measurement outcomes on different qubits taken at the same time (column vector $\mathbf{q}_m$) enables the estimation of phase difference between qubits; similarly, the analysis of correlations between measurement outcomes taken at different times on the same qubit (row vector $\mathbf{q}_n$) provides information about the temporal evolution of phases (for details, see the main text). (b) We implement correlation spectroscopy with ensembles of trapped and laser-cooled ions, such as the two-dimensional 91-ion crystal held in a monolithic ion trap shown in the picture.

Here, we study two closely related problems.

(i) We want to carry out a multiparameter estimation of the qubit-dependent phases ϕ_i in experiments where

the random phases φ_m are uniformly distributed over the interval $[0, 2\pi)$; this situation can arise if, for example, the probe time is much longer than the coherence time of the qubits. We can model this problem by preparing the qubits in

$$\rho = \frac{1}{2\pi}\int_0^{2\pi} d\varphi |\Psi(\varphi)\rangle\langle\Psi(\varphi)| \quad \text{with}$$
$$|\Psi(\varphi)\rangle = 2^{-N/2}\prod_{i=1}^{N}(|0\rangle_i + e^{i\varphi}|1\rangle_i), \tag{3}$$

a state which contains no entanglement but quantum correlations in the form of nonzero quantum discord [20,38]. Next, the qubits are subjected to the unitary operation $U_{\boldsymbol{\phi}} = \exp[(i/2)\sum_i \phi_i \sigma_i^z]$ followed by a global $\pi/2$ pulse around the x axis, $U_X = \exp[-i(\pi/4)\sum_i \sigma_i^x]$, and finally a projective measurement of all qubits is carried out in the computational basis. Given a set of measurement outcomes stored in the matrix $Q = (q_{im})$, the goal is to devise a strategy for estimating all phase differences $\phi_i - \phi_j$ with optimal precision. Note that this is a special case of a quantum sensor network [39–42], where the linear functions we wish to estimate are all the phase differences.

(ii) We are interested in characterizing the stochastic process that gives rise to temporally fluctuating random phases φ_m. Because of the symmetry of the problem in space and time as showing up in Eq. (2), a strategy for estimating the single-qubit phases ϕ_i can equally well be applied to an estimation of φ_m by analyzing the transposed matrix Q^t of measurement results.

Let us first understand the fundamental precision limits in estimating the phase differences. Given a pure product state, $2^{-N/2}\prod_{i=1}^{N}(|0\rangle_i + e^{i\phi_i}|1\rangle_i)$, and in the absence of noise, the precision in estimating each phase independently from M measurements is $\sigma_{\phi_i} = (1/\sqrt{M})$. Hence, the minimal uncertainty in estimating a phase difference $\Delta\phi = \phi_2 - \phi_1$ is

$$\sigma_{\Delta\phi} = \sqrt{\sigma_{\phi_1}^2 + \sigma_{\phi_2}^2} = \sqrt{\frac{2}{M}}. \tag{4}$$

This approach basically amounts to inferring $\Delta\phi$ from the relative phase shifts of two Ramsey fringes. Since this is the best achievable precision with a product state, we refer to it hereafter as the noiseless precision bound.

Considering $N = 2$ qubits and correlated dephasing, as in Eq. (3), the phase difference $\Delta\phi$ is estimated using standard correlation spectroscopy. Using error propagation of quantum projection noise, the uncertainty in the estimation of $\Delta\phi$ from M measurements equals

$$\sigma_{\Delta\phi}^{N=2} = \frac{\sqrt{4 - \cos^2(\phi_i - \phi_j)}}{\sqrt{M}|\sin(\phi_i - \phi_j)|}. \tag{5}$$

The uncertainty diverges when the phase difference approaches 0 or π, i.e., the points where the parity reaches an extremum. It becomes minimal for $\Delta\phi = \pi/2$, where $\min \sigma_{\Delta\phi}^{N=2} = (2/\sqrt{M})$, which is larger by a factor of $\sqrt{2}$ than the noiseless precision bound. The $\sqrt{2}$ difference in the uncertainty stems from the reduced contrast (< 0.5) in correlation spectroscopy.

For $N > 2$, one can ask whether the uncertainty of the phase difference estimation can be lowered by employing a more sophisticated analysis. Here, we provide an affirmative answer: We show that the uncertainty can be reduced by estimating the phase differences using all the $\binom{N}{2}$ pair correlations of measurement outcomes and that, in addition, a further reduction is achieved by using all the multiparticle correlations. The intuition behind this improvement is based on the following argument: An estimate of the single-qubit phase differences $\Delta\phi_{ij} = \phi_i - \phi_j$ from the observed correlations makes it possible to estimate the random phases φ_m of each experimental realization. In the limit of a large number of qubits, the near-perfect estimation of φ_m enables an "unscrambling" of the Ramsey fringes and in consequence a reconstruction of single-qubit Ramsey fringes with contrast close to 1 instead of $1/2$ as for the two-qubit parity fringe. This implies that we should be able to retrieve the noiseless precision bound of $\sigma_{\Delta\phi}^{\infty} = \sqrt{2/M}$ in the limit of $N \to \infty$.

Here, and in the remainder of this section, we assume that in the absence of correlated dephasing Ramsey fringes would have the full contrast, i.e., that there is no other source of decoherence. Later, this assumption is dropped and we also consider the influence of additional single-qubit dephasing on the measurement uncertainty. In the following, we discuss different approaches for estimation using multiqubit correlations: We start with multipair correlations and then discuss N-qubit correlations.

A. Correlation spectroscopy with many qubits: Pair correlations

Ramsey measurements of individual qubits contain no useful information, as measuring $\hat{Z}_i = |0\rangle\langle 0| - |1\rangle\langle 1|$ results in $\langle\hat{Z}_i\rangle = \mathrm{Tr}(U_X U_{\boldsymbol{\phi}}\rho U_{\boldsymbol{\phi}}{}^{\dagger} U_X^{\dagger}\hat{Z}_i) = 0$. Yet, information about transition frequency and position differences is obtained from correlation measurements [15]:

$$C_{ij} \equiv \langle\hat{Z}_i\hat{Z}_j\rangle = \frac{1}{2}\cos(\phi_i - \phi_j), \tag{6}$$

for which the correlated dephasing reduces the maximum range of correlations only by a factor of 2. A fit of the correlation matrix $C = (C_{ij})$ yields estimates $\hat{\phi}_i$ of the

single-qubit phases ϕ_i up to an irrelevant global offset phase. In experiments where $\Delta\mathbf{k} = \mathbf{k}_1 - \mathbf{k}_2 = 0$, this approach can be used to determine differences in transition frequencies up to a global sign factor. If, on the other hand, $T = 0$ and $|\Delta\mathbf{k}| \neq 0$, information about the spatial arrangement of the qubits is obtained.

B. Single-qubit phase estimates with N-particle correlations

For an estimation of the single-qubit phases $\boldsymbol{\phi} = (\phi_1, \phi_2, \ldots)$, we calculate the likelihood of observing the single-shot measurement outcome $\mathbf{q} = (q_1, \ldots, q_N)$:

$$P(\mathbf{q}|\boldsymbol{\phi}) = \frac{2^{-N}}{2\pi}\int_0^{2\pi} d\varphi \prod_{i=1}^{N}[1 + q_i \ \sin(\phi_i + \varphi)]. \quad (7)$$

Given a set of measurements $Q = (q_{im})$, a maximum-likelihood estimation of $\boldsymbol{\phi}$ is obtained via evaluation of the log-likelihood function

$$\mathcal{L}(Q|\boldsymbol{\phi}) = \log \prod_{m=1}^{M} P(\mathbf{q}_m|\boldsymbol{\phi}). \quad (8)$$

Note that the calculation of the integral in Eq. (7) can be replaced by an average over $N + 1$ evenly distributed phases $\varphi_m = 2\pi m/N$, as the highest Fourier component of the integral kernel has a period of $2\pi/N$.

C. N-particle correlations for estimating the collective random phases φ_m

Once an estimate $\hat{\phi}_i$ of the single-qubit phases is available, single-shot Ramsey spectroscopy can be used for estimating the random phase φ_m of an experimental run from the vector of outcomes $\mathbf{q}_m \equiv (q_{im})_{i=1}^{N}$. Toward this end, we calculate the likelihood function

$$P(\mathbf{q}_m|\{\hat{\phi}_i\}, \varphi) = 2^{-N}\prod_{i=1}^{N}[1 + q_{im} \ \sin(\hat{\phi}_i + \varphi)] \quad (9)$$

and use it for a Bayesian estimate of the random phase:

$$\hat{\varphi}_m = \arg\left(\int_0^{2\pi} d\varphi e^{i\varphi} P(\mathbf{q}_m|\{\hat{\phi}_i\}, \varphi)\right). \quad (10)$$

This approach allows for tracking the temporal fluctuations of the local oscillator with respect to the qubit transition frequencies. The reconstruction of the local oscillator's phase changes is unambiguous only up to integer multiples of 2π. Therefore, using this approach, the probe time has to be limited to times for which the phase diffusion is so low that phase slips are exceedingly unlikely, similar to the situation encountered when standard Ramsey spectroscopy is used.

We note that the Bayesian approach can also be applied to estimating the vector of single-qubit phases $\boldsymbol{\phi}$. Given the estimates $\hat{\varphi}_m$, the single-qubit phase differences $\Delta\phi_{ij}$ can be estimated by calculating the likelihood function

$$P(\mathbf{q}_i|\phi_i, \{\hat{\varphi}_m\}) = 2^{-N}\prod_{m=1}^{M}[1 + q_{im} \ \sin(\phi_i + \hat{\varphi}_m)], \quad (11)$$

where $\mathbf{q}_i \equiv (q_{im})_{m=1}^{M}$, in order to obtain the Bayesian estimate

$$\hat{\phi}_i = \arg\left(\int_0^{2\pi} d\phi e^{i\phi} P(\mathbf{q}_i|\{\hat{\varphi}_m\}, \phi)\right). \quad (12)$$

This approach is computationally fast albeit less precise than maximum-likelihood estimation (MLE) of $\boldsymbol{\phi}$. As discussed further below, the resulting uncertainties approach the ones obtained with maximum-likelihood estimation only in the limit of large number qubits, whereas the performance is unsatisfactory for small numbers of qubits.

III. EXPERIMENTAL IMPLEMENTATION AND MEASUREMENT RESULTS

Measurements on linear and planar $^{40}Ca^{+}$ ion crystals are performed in two different experimental setups that are described in the following.

The centerpiece of the apparatus for trapping planar crystals is a novel microfabricated monolithic linear Paul trap, shown in Fig. 2(b), which allows us to create the anisotropic potentials required for trapping 2D ion crystals while simultaneously maintaining sufficient optical access perpendicular to the crystal plane for ion imaging. The trap provides a potential in which the ions are strongly confined in the direction perpendicular to the crystal plane, at an oscillation frequency of 2.196 MHz, and weakly confined along the two other directions, in which the crystal is extended, at oscillation frequencies of about 679.8 and 343.0 kHz. Further details on this new ion trap apparatus can be found in Ref. [43]. Ions are loaded into the trap via laser ablation and are Doppler cooled on the $S_{1/2} \leftrightarrow P_{1/2}$ dipole transition. For encoding a qubit in an ion, we use the two $4S_{1/2}, m = \pm 1/2$ Zeeman ground states, coherently coupled by a magnetic radio frequency field oscillating at approximately 11.4 MHz. We distinguish the two qubit states by shelving the population of one of them in the long-lived $3D_{5/2}$ Zeeman states, followed by fluorescence detection: The qubits are measured with high fidelity by exciting the ions on the $S_{1/2} \leftrightarrow P_{1/2}$ transition and imaging the ion fluorescence onto an electron-multiplying CCD camera. For the shelving operation, we employ π pulses induced by a frequency-stable 729 nm laser, coming from a direction perpendicular to the crystal plane.

In contrast to the apparatus for manipulating 2D crystals, long strings of $^{40}Ca^{+}$ ions are trapped in a macroscopic

linear Paul trap providing a very anisotropic trapping potential with radial oscillation frequencies of about 2.5–3 MHz and an axial oscillation frequency of about 120 kHz. After Doppler cooling, the radial modes of the ion string are cooled close to the ground state by sideband cooling and the axial modes sub-Doppler cooled by polarization-gradient cooling [44]. The qubit is encoded in one of the two $4S_{1/2}$ Zeeman ground states and one of the metastable $3D_{5/2}$ Zeeman states. The ion qubit can be coherently manipulated using 729 nm laser light resonantly exciting the $S_{1/2} \leftrightarrow D_{5/2}$ transition. Two laser beams with k vectors parallel (perpendicular) to the linear ion crystal are available for collectively coupling to the qubits with the same coupling strength. Further details about this experimental setup can be found in Ref. [45].

In a first measurement, we investigate multiqubit-enhanced phase estimation in a 91-ion planar crystal; the results are shown in Fig. 3. We probe the ground-state qubits with a Ramsey probe time of 10 ms; here, magnetic-field inhomogeneities gave rise to qubit-dependent phases ϕ_i, and correlated dephasing was the result of temporal fluctuations of the magnetic field's magnitude. Figure 3(a) shows the measured pair correlations C_{ij} used for a first estimate $\hat{\phi}_i$ of the single-qubit phases shown in Fig. 3(b). Figure 3(c) displays the outcomes of an individual Ramsey experiment plotted against $\hat{\phi}_i$ together with a single-shot Ramsey fringe obtained from an estimate of the collective random phase φ_m. In Fig. 3(d), the matrix elements C_{ij} are plotted versus the improved estimate $\hat{\phi}_i - \hat{\phi}_j$ obtained by maximum-likelihood estimation based on Eq. (8), for which we maximize the likelihood by a gradient-based optimization algorithm [46]. The plot shows that the contrast of the resulting fringe is close to the maximum possible value. Similarly, averaging over experiments carried out at similar values of φ_m results in single-qubit Ramsey fringes with contrast close to 1 [Fig. 3(e)]. By subdividing the datasets into subsets of 200 measurements each, it is possible to measure the uncertainty of the phase difference estimates $\hat{\phi}_i - \hat{\phi}_j$. Pink data points in Fig. 3(f) show the uncertainty based on estimating the phase difference from the pair correlation between two qubits, which becomes minimal for a phase difference of $\pi/2$. The measured uncertainties are in agreement with the bound provided by quantum projection noise in the presence of correlated dephasing. The lowest uncertainty is obtained by maximum-likelihood estimation using N-qubit correlations (blue data points and blue line, average over all points). The dashed line is the lower bound in the limit of $M \to \infty$ and $N \to \infty$.

The same dataset can also be used for investigating the measurement uncertainties as a function of the number of qubits as shown in Fig. 4. Toward this end, we split the data into subsets, each containing a fixed number of qubits with single-qubit phases that are approximately evenly distributed over the interval $[0, 2\pi)$. The measurements of each of these sets is further split into subsets containing $M = 200$ experimental realizations from which we reconstruct the single-qubit phases for an estimate of the measurement uncertainties. Dark blue data points represent reconstructions based on MLE [Eqs. (7) and (8)], and light blue points are the results of the noncompetitive Bayesian approach [Eqs. (11) and (12)]. As shown in Sec. IV, the uncertainties of the MLE estimates can be fitted by Eq. (17) with a fringe

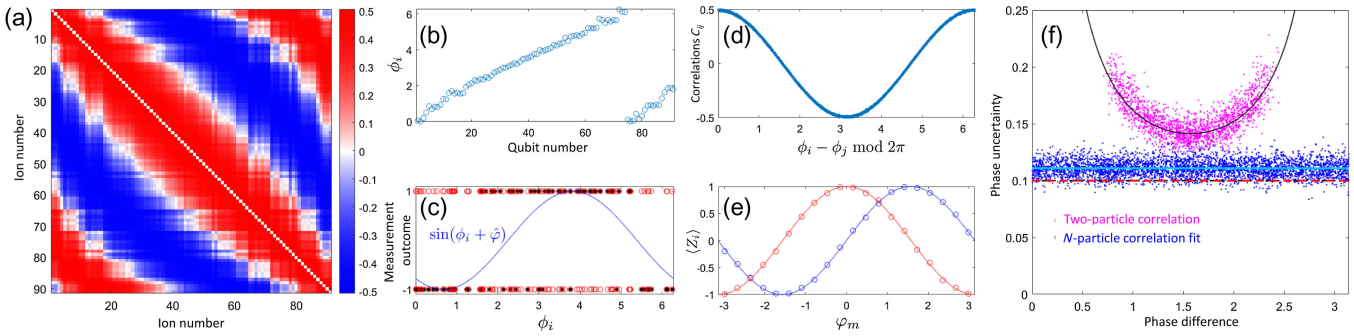

FIG. 3. Many-qubit correlation spectroscopy of a 91-ion planar crystal based on $M = 26852$ experimental repetitions. (a) Measured correlation matrix with correlations $|C_{ij}| \leq 1/2$ limited by correlated dephasing. (b) Single-qubit phases $\hat{\phi}_i$ estimated by fitting the correlation matrix. (c) Measurement outcomes q_{im} of an individual experiment (black dots) used for a Bayesian estimate of the common random phase $\hat{\varphi}_m$ (blue curve, fitted Ramsey fringe). (d) Correlation matrix elements C_{ij} plotted as a function of the phase difference $\phi_i - \phi_j$ obtained by analyzing N-qubit correlations. (e) Single-qubit Ramsey fringes with nearly full contrast obtained from binning into sets of similar common random phase φ_m modulo 2π. The red and the blue curve are just two out of 91 measured fringes. (f) Measurement uncertainties inferred from subdividing the data into 134 data sets with 200 repetitions each. The pink dots do not cover the entire range of 0 to π, as we omit those qubit pairs (i, j) for which we measure $|C_{ij}| > 0.5$ for one or several subsets. Uncertainties obtained from individual elements C_{ij} (pink dots) and the analysis of N-qubit correlations (blue dots and solid light blue line, average over the data points). The dashed red line indicates the noiseless precision bound achievable in the limit of $N \to \infty$, the solid black line the two-qubit limit $\sigma_{\Delta\phi}^{N=2}$.

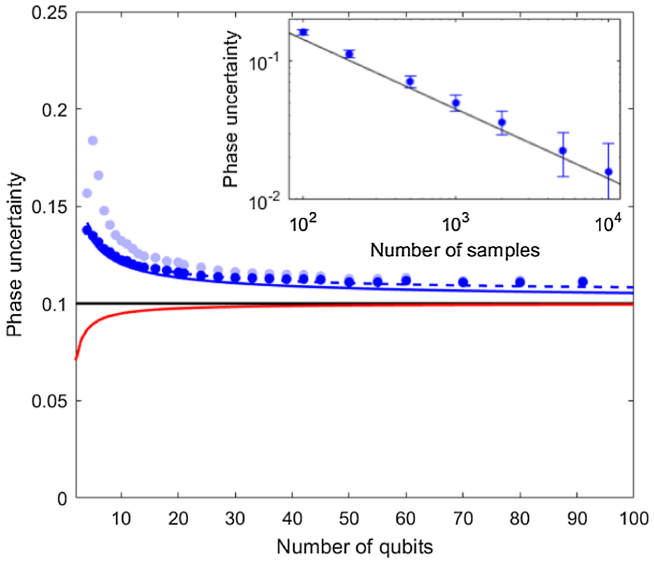

FIG. 4. Phase uncertainties versus number of qubits for $M = 200$ samples. Dark blue dots represent uncertainties estimated from experimental data by MLE, light blue dots the uncertainties of the Bayesian estimation. The prediction of Eq. (17) is shown as the solid blue curve for a contrast $C_0 = 1$ and as a dashed blue curve for $C_0 = 0.995$. The latter is obtained by fitting the experimental data. The black curve represents the noiseless precision bound of $\sqrt{2/M}$. The red curve represents the optimum uncertainty that is obtainable with entangled input states (see Appendix C). The reduction in measurement uncertainty provided by preparation of entangled input states rapidly shrinks with increasing N. The inset displays the measured uncertainty for $N = 91$ on the number samples, with the black curve representing the noiseless precision bound.

contrast of $C_0 = 0.995$, which could result from state-assignment errors and slow drifts of trap parameters over the duration of the measurement. The inset shows that the phase uncertainty decreases inversely proportional to the number of samples in a given set and is, thus, still projection-noise limited at $M = 10^4$ samples. Note that we use an unbiased estimator for the determination of the uncertainties displayed in Figs. 3 and 4 assuming normally distributed measurement results [47].

IV. BOUNDS TO THE ACHIEVABLE PHASE ESTIMATION UNCERTAINTY

In this section, we compare the experimentally measured uncertainties to the theoretically achievable minimum uncertainties for an unbiased estimator and M experimental samples. The noiseless precision bound $\sqrt{2/M}$ in Eq. (4) cannot be experimentally achieved, as it assumes noiseless dynamics, i.e., that the single-qubit Ramsey fringes [cf. Fig. 3(e)] can be measured with unity contrast. However, this assumption is unrealistic in noisy experiments affected by strong correlated dephasing and small levels of single-qubit dephasing.

The impact of these two noise sources on the precision is different. Uncorrelated dephasing reduces the fringe contrast to $C_0 < 1$, which unavoidably degrades the precision. In contrast, the effect of strong correlated dephasing can be overcome with a suitable data analysis for a large number of ions. This can be understood as follows: Given a large number of ions, the random phase in each shot, φ_m, can be estimated with an error that goes to zero as $N \to \infty$. Another way to understand this is that for correlated dephasing there are decoherence-free subspaces (unlike the case of uncorrelated dephasing). The density matrix has elements inside and outside the decoherence-free subspaces, and as $N \to \infty$ the contribution of the elements outside the protected subspaces goes to zero. Here, we take these factors into consideration. We derive heuristic precision bounds that depend on both the number of qubits N and a finite Ramsey contrast C_0 (in the absence of correlated dephasing). We start with a simple analytical model for an estimator based on N-particle correlations and compare the predictions to numerical simulations based on the classical Fisher information.

A. Measurement uncertainties with N-particle correlations

Here, we derive a simple analytic model to approximate the precision bounds given correlated and uncorrelated dephasing.

Before we proceed to the model, let us first understand the effect of uncorrelated dephasing and generalize the noiseless precision bound to a finite contrast limit that takes into account this dephasing and serves as a similar benchmark. Given an uncorrelated dephasing, the product state mentioned in Sec. II becomes a mixed state: $(1/2^N)\prod_i (\mathrm{I} + C_0\hat{R}_{\phi_i})$, with $\hat{R}_{\phi_i} = \cos(\phi_i)\hat{X}_i + \sin(\phi_i)\hat{Y}_i$. Measuring the ith qubit in the $\hat{Y}_i$ basis, the probability of 1 is $p = \frac{1}{2}(1 + C_0 \sin(\phi_i))$. Then, the uncertainty in the determination of p with M repetitions is given by projection noise, $\sigma_p = \sqrt{p(1-p)/M}$. Because of $\sigma_p = |dp/d\phi_i|\sigma_{\phi_i}$ and $(dp/d\phi_i) = (C_0/2)\cos(\phi_i)$, we have $\sigma_{\phi_i} = (1/\sqrt{N_{\mathrm{eff}}(C_0, \phi_i)})$, where

$$N_{\mathrm{eff}}(C_0, \phi_i) = MC_0^2 \frac{(1 - \sin^2\phi_i)}{1 - C_0^2 \sin^2\phi_i} \tag{13}$$

is an effective number of measurements. Assuming ϕ_i is drawn from a uniform distribution, the uncertainty becomes $\sigma_{\phi_i} = (1/\sqrt{N_{\mathrm{eff}}(C_0)})$ with

$$\begin{aligned} N_{\mathrm{eff}}(C_0) &= \frac{1}{2\pi}\int_0^{2\pi} d\phi_i\, N_{\mathrm{eff}}(C_0, \phi_i) \\ &= M\left(1 - \sqrt{1 - C_0^2}\right). \end{aligned} \tag{14}$$

The uncertainty in estimating $\Delta\phi = \phi_i - \phi_j$ is $\sqrt{\sigma_{\phi_i}^2 + \sigma_{\phi_j}^2}$ and, thus, equal to

$$\sigma_{\Delta\phi} = \frac{\sqrt{2}}{\sqrt{M}\sqrt{1-\sqrt{1-C_0^2}}}. \tag{15}$$

Since this is the minimal obtainable uncertainty given a contrast of C_0 and assuming no correlated dephasing, we refer to it as the finite contrast precision bound.

We derive now a simple model for precision bounds given also correlated dephasing. The idea is to first find the uncertainty in estimating the common random phase φ_m and then insert this uncertainty as an uncorrelated dephasing of each qubit.

We first need to find the uncertainty in estimating φ_m (given that all the other phases are known). Note that this is exactly the same calculation as performed above for ϕ_i, just taking $M = N$; therefore, $\sigma_{\varphi_m} = (1/\sqrt{N}\sqrt{1-\sqrt{1-C_0^2}})$. This limits the precision with which the random phases φ_m can be estimated. We can, thus, take the distribution of the random phase to be Gaussian with this variance. By averaging the single-qubit probability over the Gaussian distribution $\mathcal{N}(\varphi_m, \sigma^2)$,

$$\langle \cos(\phi_i + \varphi)\rangle_{\mathcal{N}(\varphi_m,\sigma^2)} = \cos(\phi_i + \varphi_m)\exp\left(-\frac{\sigma^2}{2}\right),$$

we observe that the contrast of the unscrambled single-qubit Ramsey fringe [Fig. 3(e)] gets reduced to

$$C_{\text{unscr}} = C_0 \exp\left(-\frac{1}{2N(1-\sqrt{1-C_0^2})}\right), \tag{16}$$

if C_0 was the Ramsey contrast in the absence of correlated dephasing. We can now apply the same reasoning again to estimate the uncertainty with which the shift of unscrambled Ramsey fringes can be determined in order to estimate the uncertainty of the phase difference $\phi_i - \phi_j$ which becomes

$$\sigma_{\Delta\phi}(N, C_0) = \frac{\sqrt{2}}{\sqrt{M(1-\sqrt{1-C_{\text{unscr}}^2})}}. \tag{17}$$

For the case of large qubit number and high contrast C_0, this expression can be approximated by Eq. (15) if the replacement $C_0 \to C_0 \exp[-(1/N)]$ is made.

B. Fisher-information-based bounds

We use a Fisher information (FI) analysis to calculate the achievable minimum uncertainties. According to the Cramer-Rao bound, the Fisher information matrix sets a bound on the achievable uncertainty with any unbiased estimator

$$\text{COV}(\boldsymbol{\phi}) \geq I^{-1}, \tag{18}$$

where COV is the covariance matrix of the parameters $\boldsymbol{\phi} = (\phi_i)$ and I^{-1} is the inverse of the FI matrix. In case I is singular, i.e., information can be obtained only about a subspace of the parameters, I^{-1} is the Moore-Penrose pseudoinverse, defined only on this subspace. This implies that the variance of the phase difference $\phi_i - \phi_j$ is given by

$$\text{Var}(\phi_i - \phi_j) \geq \mathbf{v}_{ij}^t I^{-1} \mathbf{v}_{ij}, \tag{19}$$

where $\mathbf{v}_{ij}$ is a column vector with components $(\mathbf{v}_{ij})_n = \delta_{\text{in}} - \delta_{jn}$ and I^{-1} the inverse of the relevant FI matrix.

The Fisher information matrix $I = (I_{ij})$ can be calculated by the following formula:

$$I_{ij} = \sum_k p_k^{-1}(\boldsymbol{\phi}) \frac{\partial p_k(\boldsymbol{\phi})}{\partial \phi_i} \frac{\partial p_k(\boldsymbol{\phi})}{\partial \phi_j}, \tag{20}$$

where $\boldsymbol{\phi} = (\phi_i)$ is the vector of parameters and p_k the probability distribution of the observations. As a simple example, observe that, for a single-parameter Bernoulli distribution $p(\phi)$, the FI about ϕ is $I = (\partial_\phi p)^2/p(1-p)$ and, hence, $\sigma_\phi = \sqrt{p(1-p)}/\partial_\phi p$. Given M identical independent Bernoulli trials, the FI about ϕ is multiplied by a factor of M and, thus, $\sigma_\phi = \sqrt{p(1-p)}/\sqrt{M}\partial_\phi p$. This expression coincides with the uncertainty of Eqs. (4) and (5). Furthermore, note that the FI is a generalization of N_{eff} defined in Sec. IV A.

1. Fisher information bound for the pair correlations

In pair correlation analysis, we estimate the ion phases (ϕ_i) using the pair correlations of the measurement outcomes, i.e., the correlation matrix $C_{i,j}$ defined in Eq. (6) and presented in Fig. 3(a). More precisely, we take the averages

$$\left\{\frac{1}{M}\sum_{m=1}^{M} q_{i,m} q_{j,m}\right\}_{i\neq j}$$

and estimate the phases according to it. According to the central limit theorem, the averages converge to a Gaussian random variable $\mathcal{N}((\mu_{i,j})_{i\neq j}, M^{-1}\Sigma)$, where $\mu_{i,j} = \langle q_i q_j\rangle = \frac{1}{2}C_0^2\cos(2(\phi_i - \phi_j))$ and Σ is the covariance matrix $\Sigma_{(i,j),(k,m)} = \langle q_i q_j q_k q_m\rangle - \langle q_i q_j\rangle\langle q_k q_m\rangle$. An explicit calculation of the covariance matrix elements is presented in Appendix A.

Since the distribution is normal, the FI matrix about (ϕ_i) is given by [48]

$$I = (\partial_\phi \boldsymbol{\mu})^\dagger \Sigma^{-1} (\partial_\phi \boldsymbol{\mu}). \tag{21}$$

$(\partial_{\boldsymbol{\phi}}\boldsymbol{\mu})_{i,(k,m)} = \partial_{\phi_i}\mu_{k,m}$ is the information gained due to the change in the mean values, i.e., the signal, and Σ is the covariance matrix of the different correlations representing the noise.

Applying Eq. (21) for a single-pair correlation (i,j), we retrieve the uncertainty in Eq. (5): The only linear combination of ϕ_i and ϕ_j that has a nonvanishing FI is $\phi_i - \phi_j$, for which the FI is $\sin^2(\phi_i - \phi_j)/4 - \cos^2(\phi_i - \phi_j)$, i.e., $\sigma_{\Delta\phi} = (\sqrt{4 - \cos^2(\phi_i - \phi_j)}/|\sin(\phi_i - \phi_j)|)$. The minimal uncertainty per measurement is 2, and a divergence occurs for $\phi_i - \phi_j = n\pi (n \in \mathbb{Z})$ due to the vanishing derivative and nonvanishing noise.

Since information about $\phi_i - \phi_j$ is encoded not only in the (i,j) correlations but in other pairs as well, using all pairs improves the uncertainty and removes the divergence around $n\pi$. We use Eq. (21) to perform an exact numerical calculation of the FI. The behavior of the FI is presented in Figs. 10 and 11 in Appendix A. It can be seen from the figures that as $N \to \infty$ the FI with pair correlations does not saturate the noiseless precision bound. The reason for this is the information encoded only in higher moments. Using an analytical approximation, we show in Appendix A that the variance for large N converges to $4 - C_0^2/C_0^2$, while the finite contrast precision bound to the variance is $2/1 - \sqrt{1 - C_0^2}$. As C_0 gets smaller, the variance with pair correlations gets closer to this bound, since the information from higher moments becomes smaller.

2. Fisher information bound with N-particle correlations

When using the full counting statistics, the probability distribution entering into the calculation of the Fisher information matrix is given by Eq. (7) with the replacement $q_i \to C_0 q_i$ in order to account for a Ramsey contrast $C_0 < 1$. In Appendix A, we numerically calculate the Fisher information matrix for finding the lower limit to the achievable uncertainty as a function of qubit number N and contrast C_0 (see Fig. 11). When N becomes large, an exact evaluation of the Fisher information matrix by Eq. (20) becomes impractical, as a summation over 2^N terms would have to be carried out. For $N > 24$, we sample bit strings from the underlying probability distribution for a Monte Carlo calculation of the empirical Fisher information matrix. The uncertainty achievable in experiments with a finite number of repetitions is numerically investigated in Appendix B.

3. Improving precision limits using entanglement

In our experiments, the qubits are initialized to a product state and measured in a local X basis. Hence, no entanglement occurs in these experiments, and an analysis based on classical Fisher information suffices. This raises the question of whether nonclassical protocols that involve entangled states or different measurement bases can yield an advantage. It turns out that this is indeed the case: More general quantum protocols can obtain the noiseless precision bound of $\sqrt{2/M}$ with an initial product state for every N, and with an entangled initial state we can further reduce the uncertainty to $\sqrt{N-1/N}\sqrt{2/M}$. We prove in Appendix C that this uncertainty is optimal.

To obtain these results, we use the quantum Fisher information (QFI), which is the FI optimized over all possible measurement strategies [49,50]. After averaging the quantum state over the random phase [Eq. (3)], we show that the noiseless precision bound can be achieved for every N with a suitable measurement strategy (see Appendix C 1). To gain intuition, let us examine the case of $N = 2$: When measuring in the local X basis, Eq. (5) predicts $\sigma_{\Delta\phi} \geq (2/\sqrt{M})$. However, if we first measure the total number of excitations, i.e., $Z_1 + Z_2$, and then measure in the local X basis, the noiseless precision bound of $\sqrt{2/M}$ is achieved.

Optimizing over both initial states and measurement strategies, we prove in Appendix C 2 that the ultimate precision limit is $\sqrt{N-1/N}\sqrt{2/M}$. Several initialization strategies saturate this bound; in particular, any initial pure state with $\langle Z_j\rangle = 0, \langle Z_j Z_k\rangle = -(1/N-1)$ for all $j \neq k$ achieves it. The reason for this improvement is the minimal $\sum_{j\neq k}\langle Z_j Z_k\rangle$, which guarantees minimal uncertainty. The reason this limit grows with N is frustration: One cannot make all pairs of spins antiparallel. While the number of pairs is $\binom{N}{2}$, the minimal $\sum_{j<k}\langle Z_j Z_k\rangle$ is $-N/2$, and, thus, the optimal $\langle Z_j Z_k\rangle$ is $-(1/N-1)$.

It can be immediately observed that the symmetric Dicke state with $N/2$ excitations satisfies these conditions and, thus, is optimal. Another optimal strategy is to employ a probabilistic initialization to products of antiparallel Bell states; i.e., in each experiment, different pairs are being entangled to form an antiparallel Bell state. With these two initialization strategies, the optimal sensitivity can be achieved with local measurements in the X or Y basis. This bound is plotted as a red curve in Fig. 4 along with other theoretical limits. A detailed derivation of the bound and the required initial states and measurements is presented in Appendix C 2.

These theoretical quantum limits imply that some improvement can indeed be obtained using entangled states or nonlocal measurements; however, this improvement becomes negligible in the limit of a large number of ions. This potential improvement and a comparison between the different precision limits are presented in Fig. 4.

V. APPLICATIONS IN TRAPPED-ION EXPERIMENTS

In the following, different applications of correlation spectroscopy in trapped-ion experiments are presented.

A. Measurement of ion positions

Very anisotropic potentials are required for confining many ions in the form of a linear string. As a consequence

of the weak axial confinement, these strings have lengths that are no longer small as compared to the distance between the ions and the nearest trap electrode. Therefore, the trapping potential can no longer be modeled as being purely harmonic, and anharmonicities, which might affect the ion string's normal modes of motion, have to be considered.

We reconstruct the trapping potential in the axial direction by Ramsey experiments probing an optical qubit on the $S_{1/2} \leftrightarrow D_{5/2}$ transition, in which the first (second) $\pi/2$ pulse is realized by a laser beam impinging on the ions from the axial (perpendicular) direction. This setting results in qubit-specific phases $\phi_i = kx_i$, where k is the wave number and x_i denotes the coordinate of the ith ion along the direction of the ion string. To suppress energy-dependent phase contributions, we use short $\pi/2$ pulses without any free-evolution time in between. Following the previously outlined procedure, we first reconstruct the qubit phase ϕ_i and the measurement contrast by fitting the correlation matrix. Next, we use these phases for reconstructing the time-dependent random phases φ_m. Using N-qubit correlations, we finally use the Bayesian approach of Eq. (12) for an improved phase estimate of ϕ_i, shown as open symbols in Fig. 5(a) for a string of 62 ions.

In a second step, we extract the trapping potential from the measured correlations. We approximate the potential by Taylor expanding it up to fourth order, $V(z) = \frac{1}{2}m\omega_0^2 z^2[1 + z/l_3 + (z/l_4)^2]$, where ω_0 is the oscillation frequency of a single ion and l_3 (l_4) account for the cubic (quartic) anharmonicity of the potential. By calculating the ion positions in this potential, we fit the measured ϕ_i and find $\omega_0 = (2\pi)109.728(3)$ kHz, $l_3 = 2.1(7)$ mm, and $l_4 = 0.8(6)$ mm, where the error bars are obtained from

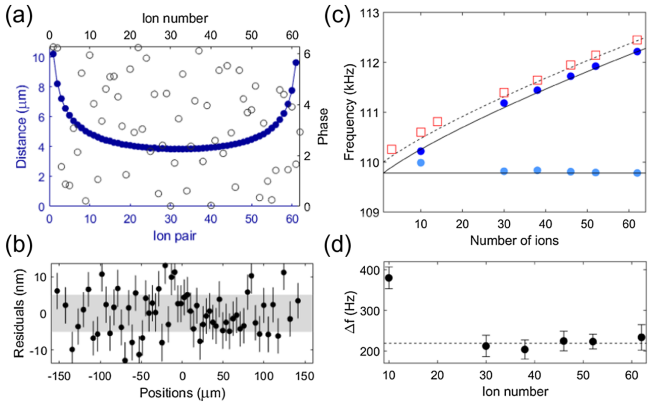

FIG. 5. (a) Reconstruction of the axial trapping potential. (a) Measured phases ϕ_i (open symbols) and nearest-neighbor distances (full symbols) obtained by fitting a model potential. (b) Residuals. Shaded area: theoretical minimum measurement uncertainty. (c) Center-of-mass mode frequency measured by correlation spectroscopy, $\omega_c/(2\pi)$ (dark blue circles) and by sideband spectroscopy, $\omega_{sb}/(2\pi)$ (squares) versus number of ions, together with the fitted value of $\omega_0/(2\pi)$ (light blue circles). (d) Measured $(\omega_{sb} - \omega_c)/(2\pi)$.

nonlinear regression assuming quantum projection noise as the only source of errors. We compare the measured phases ϕ_i to the ones obtained from fitting the potential (ϕ_i^{fit}) by calculating the residual position errors $\delta x_i = (\phi - \phi_i^{\mathrm{fit}})/k$. Figure 5(b) shows that these residuals have a standard deviation of 6.0 nm, barely above the theoretically expected error $\sigma_{\Delta\phi} = 5.1$ nm. Moreover, the absence of spatial correlations in the residuals demonstrates that Taylor expanding the potential up to the fourth order is an adequate approximation to the exact potential.

To further test the method, we carry out the reconstruction of the potential for a fixed set of trap parameters but different number of ions ($10 \leq N \leq 62$) and obtain consistent results. Figure 5(c) shows the inferred oscillation frequency ω_0 (light blue points) and the lowest collective mode frequency ω_c (dark blue points). For an independent cross-check, the latter is also measured via sideband spectroscopy on the $S_{1/2}$ to $D_{5/2}$ transition (red squares). We observe that the correlation measurement systematically underestimates the mode frequency by about 220 Hz [Fig. 5(d)]. This discrepancy could be explained by the perpendicular laser beam being misaligned by about 1 mrad. Apart from this systematic error, the match between the two methods is quite good for $N > 10$ ions: The inset shows the difference of the predicted mode frequencies, which have a standard deviation of only 14 Hz if the $N = 10$ data point is excluded on the basis of the rather uneven distribution of the phases ϕ_i over the interval from 0 to 2π. Systematic effects in the measured frequencies by imperfect laser beam misalignment could be further reduced by replacing the perpendicular beam by another axial beam that is counterpropagating to the axial beam in place, because small alignment errors of the beams with the direction of the ion string would affect the measurement outcomes only in second order.

B. Measurement of transition frequency differences

Correlation spectroscopy with long probe times provides a tool for precisely measuring spatial transition frequency variations, which are relevant for frequency standards and quantum simulation experiments. For $^{40}Ca^+$ ions, the dominant frequency shifts are Zeeman and electric quadrupole shifts. We measure the spatial dependence of these shifts by probing the stretched $S_{1/2}, m = \pm 1/2 \leftrightarrow D_{5/2}$, $m = \pm 5/2$ transitions with a Ramsey time of $\tau = 40$ ms duration with a 51-ion string. In contrast to the experiments of Sec. V A, both Ramsey pulses are realized by the same laser beam. Writing the spatially resolved shifts $\Delta_i^{\pm}$ as $\Delta_i^Q = (\Delta_i^+ + \Delta_i^-)/2$ and $\Delta_i^B = (\Delta_i^+ - \Delta_i^-)/2$ enables a separation of electric quadrupole and magnetic-field shifts.

Figures 6(a) and 6(b) display the measured quadrupole shift together with a calculated shift obtained from a measurement of the ion positions and the known quadrupole moment $\theta(3d, 5/2)$ of the $D_{5/2}$ level [26]. The

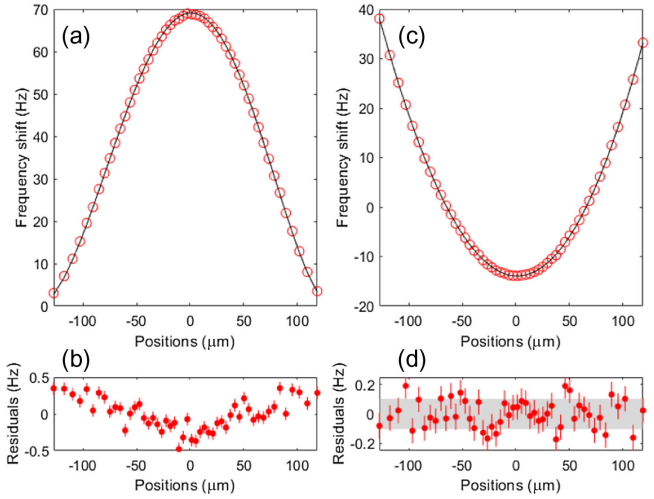

FIG. 6. Transition frequency shift measurement obtained by probing the quadrupole transitions between stretched states with 1500 experimental repetitions each. (a) Quadrupole shift of the $D_{5/2}, m = \pm 5/2$ states (red circles, measured shift; black line, predicted shift). The frequency shift is measured with respect to the first ion; in the figure, a constant offset is added so that the averaged shift equals the calculated average quadrupole shift. (b) Measurement residuals. (c) Differential Zeeman shift of the $S_{1/2}, m = 1/2 \leftrightarrow D_{5/2}, m = 5/2$ transition frequency. An offset is added so that the average shift becomes equal to zero. The black line is a fit to the data by a third-order polynomial. (d) Residuals. The gray rectangle indicates the measurement uncertainty (1σ) predicted for quantum projection noise.

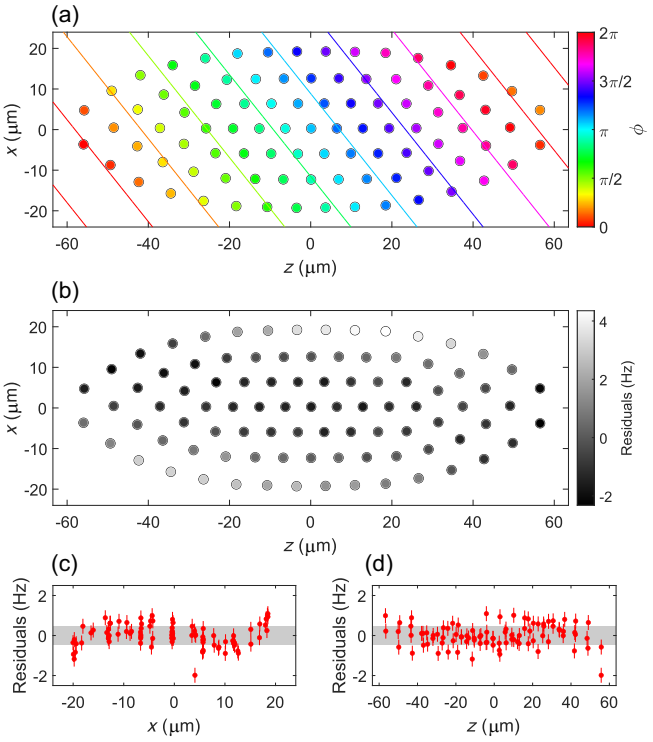

FIG. 7. Transition frequency shift measurement in a two-dimensional crystal obtained by probing the ground-state transition with 19 736 experimental repetitions. (a) Single-ion phases together with contour lines of constant phases obtained from a linear fit. (b) Residuals from the linear fit. (c),(d) Residuals from the quadratic fit along the (c) x and (d) z axis. The gray rectangle indicates the 1σ measurement uncertainty predicted for quantum projection noise.

systematic variation of the residuals on the scale of 0.5 Hz could be explained by a 1.5σ error in the determination of $\theta(3d, 5/2)$ or by a misalignment of the perpendicular laser beam by 3 mrad. Figures 6(c) and 6(d) display the level shifts by the inhomogeneous magnetic field produced by the permanent magnets defining the quantization axis. We fit the Zeeman shifts with a third-order polynomial of the ion positions in order to extract the residuals. The latter have a standard deviation of 109 mHz, approaching the minimal uncertainty of 103 mHz predicted by the noiseless limit.

Figure 7(a) shows the measured single-ion phases for a two-dimensional 91-ion crystal in the presence of a spatially varying magnetic field. We probe the ground-state transition $S_{1/2}, m = -1/2 \leftrightarrow S_{1/2}, m = +1/2$ by a Ramsey experiment of $\tau = 5$ ms duration. We fit a linear function to the measured phases and show the contour lines of constant phases from the fit in Fig. 7(a). We extract a magnetic-field gradient of 0.85(1) G/m from the linear fit with an angle of 38.6(4)° with respect to the horizontal direction. The maximal measured transition frequency difference between the ions is 218.2(8) Hz. The spatial distribution of the residuals from the linear fit, shown in Fig. 7(b), reveals that the magnetic field contains higher-order terms in addition to the linear gradient. We further fit a quadratic function to the residuals and show the remaining residuals in Figs. 7(c) and 7(d) along the two orthogonal directions. The majority of the spatial structure in the magnetic field can be explained with linear and quadratic terms, as the remaining residuals show almost no systematic structure. Experimentally, it is straightforward to cancel linear variations of the magnetic field across the ion crystal with permanent magnets or coils placed outside the vacuum system.

C. Single-shot Ramsey interferometry

The data taken for probing the spatial dependence of phase shifts can also be analyzed in the time domain: We probe temporal fluctuations of the local oscillator's phase at the locations of the ions by single-shot Ramsey interferometry. Figure 8 shows examples of such temporal phase changes that are caused by magnetic-field fluctuations, laser frequency noise, and optical path length fluctuations, respectively. Figure 8(a) shows a magnetic-field change of about 3 μG at the location of the ions induced by the arrival of an elevator at the lab floor. The magnetic field is sensed by a 49-ion string probed by a 40 ms Ramsey experiment on the Zeeman ground state qubit transition. For the data shown in Fig. 8(b), the $S_{1/2}, m = 1/2 \leftrightarrow D_{5/2}, m = 3/2$

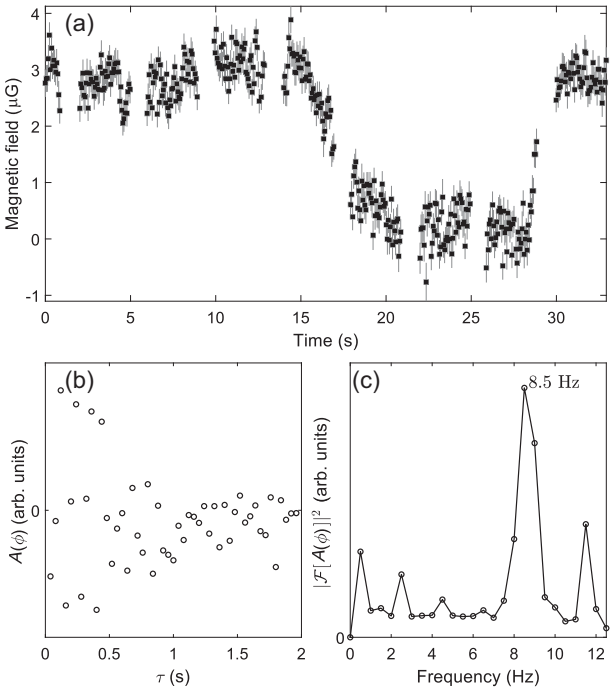

FIG. 8. Single-shot Ramsey interferometry tracking temporal phase fluctuations. (a) Phase fluctuations induced by a time-varying magnetic field probed with a 49-ion string. (b),(c) Tracking laser frequency variations with a 51-ion string: autocorrelation function $A(T)$ of laser phase fluctuations (left) together with its spectral density $|\mathcal{F}[A(T)]|^2$ (right).

transition is probed for $\tau = 20$ ms. Here, 371 data points are acquired, each containing 50 experiments that are recorded at a repetition rate of 25 Hz. Laser phase noise gives rise to phase fluctuations for which an autocorrelation is calculated. The spectral density of the autocorrelation function reveals distinct components at low frequencies

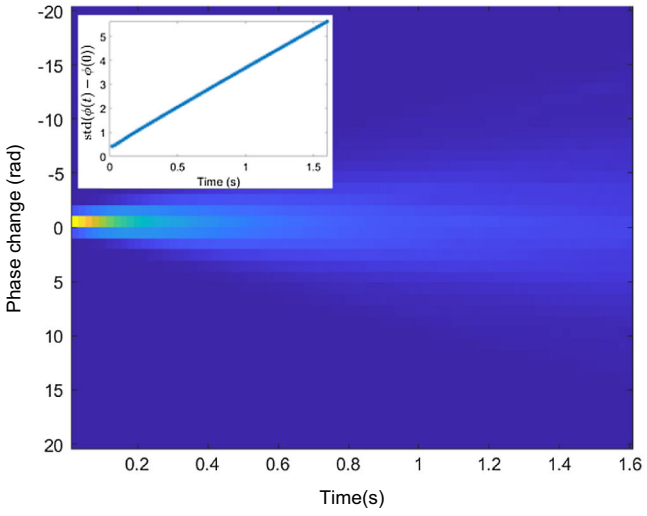

FIG. 9. Measurement of temporal relative optical path length fluctuations in two beam path delivering the laser pulses to a string of 40 ions.

contributing to the laser noise. The dominant component at approximately 8 Hz introduces a frequency excursion on the order of 1 Hz. Figure 9 shows differential path length fluctuations in the time domain, measured with short Ramsey experiments using two different laser beam paths for the two Ramsey pulses. For durations below 2 s, the data show phase fluctuations $\langle[\varphi(t+\tau)-\varphi(t)]^2\rangle_t$ between experiments separated by a time τ that increase in proportion to τ as shown in the inset. The phase diffusion is predominantly caused by path length fluctuations in the two optical fibers delivering the light to the ion trap.

VI. DISCUSSION AND OUTLOOK

We have investigated many-qubit correlation spectroscopy for probing qubits subjected to spatially correlated noise. The technique enables phase comparisons between any pair of qubits, provided that the qubit states are about evenly distributed over the equatorial plane of the Bloch sphere. The latter condition does not impose a strong restriction, as in most experimental setups it should be possible to deliberately imprint spatial phase gradients on the qubit array to satisfy this requirement. While single-pair correlation limits the contrast to 50%, in the limit of large qubit number and perfectly correlated noise, the multiqubit correlations induced by the noise enable a nearly complete restoration of the Ramsey contrast. The increased contrast gives rise to a fourfold reduction in measurement time needed to achieve the targeted measurement uncertainty.

Many-qubit correlation spectroscopy is easy to implement, as it requires only standard Ramsey spectroscopy enhanced by single-qubit readout. The technique is, therefore, not limited to trapped-ion experiments but could be used in any multiqubit physical system with high-fidelity single-shot readout of individual qubits. In particular, it might be applicable to atomic clock experiments in tweezer arrays. Recently, experiments applying Ramsey correlation spectroscopy to subensembles of atoms held in optical lattices or tweezer arrays have demonstrated very small frequency gradients and impressive optical atomic coherence times reaching tens of seconds [25,51,52]. In one- or two-dimensional tweezer arrays, which feature single-atom detection of tens to hundreds of atoms [25,31,53], our method is directly applicable and could assist in reducing the measurement time required for characterizing spatially varying transition frequency shifts across the atomic array. With the further development of atomic clocks networks connected by phase-stable photonic links [54,55], multiqubit correlation spectroscopy could be applied for mutual frequency comparisons of the clocks, too. Another application of the technique might be found in quantum information processing experiments where spatially correlated noise can degrade the device performance. For example, in the atomic tweezer experiments reported in Ref. [31], an auxiliary atomic species was employed for sensing and in-sequence correction of correlated phase

noise. Here, an application of our protocol to the sensing species might increase the maximum noise level for which the correction can still be applied.

In the context of trapped-ion experiments, many-qubit correlation spectroscopy proves to be a valuable tool for characterizing various aspects of the experimental setup with high precision. Our experiments demonstrate that experimentally observed uncertainties come close to the theoretically predicted ones. The resulting reduction in measurement time for achieving a desired uncertainty could be of interest for tracking the frequency of an unstable laser and providing feedback from individual measurements for improving its stability. Another application of multiqubit correlation spectroscopy, which we did not explore in this paper, is to use it for thermometry and detection of structural phase transitions in ion crystals [56,57]. In this context, insufficiently cooled (low-frequency) motional modes could give rise to a reduction of fringe contrast that could be detected in correlation spectroscopy experiments.

While in our experiments both the readout and the initial states are nonentangled, we have theoretically shown the possibility of improving the precision using an entangled initial state or nonlocal measurements. While being negligible for large N, this improvement can be considerable assuming a relatively small N. A possible experimental realization requires initialization to a symmetric Dicke state. In trapped-ion experiments, these Dicke states could be engineered [58] by preparing the ions' center-of-mass mode in a Fock state with $N/2$ quanta, followed by a rapid adiabatic passage on its red-sideband transition [59], which converts motional quanta into collective electronic excitations [60]. Finding simple protocols for generating optimal initial states and implementing these protocols in a sensing experiment is an interesting challenge for future work.

In view of experiments with multiple atomic ensembles, each of which can be measured only collectively, we generalized the multipair correlation method to an arbitrary spin J, that could represent the collective Bloch vector of $N = 2J$ atoms. As shown in Appendix D, an analysis of single-pair correlation performs poorly in the limit of large spins, since the resulting uncertainty cannot surpass $1/\sqrt{2}$. However, when jointly analyzing all pair correlations, a sensitivity of $\sqrt{3/2J}$ is obtained. This analysis could be particularly relevant to Ramsey experiments with global readout of multiple ensembles of qubits [51,52,61]. The ellipse fitting method is typically used in these experiments, and care needs to be taken to avoid biased phase estimation [52]. We posit that our analysis could improve on the ellipse fitting technique in the limit of multiple ensembles containing a few qubits each.

All data presented in Fig. 3 and subsequent figures are available online [62].

ACKNOWLEDGMENTS

We acknowledge useful discussions with Alex Retzker. The project leading to this application has received funding from the European Research Council (ERC) under the European Union's Horizon 2020 research and innovation program (Grant Agreement No. 741541) and from the European Union's Horizon 2020 research and innovation program under Grants Agreement No. 817482 and No. 101113690. Furthermore, we acknowledge support by the Austrian Science Fund through the SFB BeyondC (Grant-DOI 10.55776/F7110) and funding by the Institut für Quanteninformation GmbH. This project has received funding from the European Union's Horizon 2020 research and innovation program under the Marie Skłodowska-Curie Grant Agreement No. 801110 and the Austrian Federal Ministry of Education, Science and Research (BMBWF). T. G. acknowledges funding provided by the Institute for Quantum Information and Matter and the Quantum Science and Technology Scholarship of the Israel Council for Higher Education.

APPENDIX A: BOUNDS TO THE ACHIEVABLE PHASE ESTIMATION UNCERTAINTY

1. Pair correlations

We analyze the Fisher information obtained using only pair correlations. As mentioned in the main text, the relevant random variables are the pair correlations

$$\left\{\frac{1}{M}\sum_{m=1}^{M} q_{i,m}q_{j,m}\right\}_{i,j>i} \to \mathcal{N}(\{\mu_{i,j}\}_{i,j>i}, \Sigma), \quad \text{(A1)}$$

which, according to the central limit theorem, converge to a Gaussian distribution, where $\mu_{i,j}$ is the average of $q_i q_j$ and Σ is the covariance matrix of the $\{q_i q_j\}_{i,j>i}$.

Hence, the problem boils down to calculating the FI matrix for this Gaussian distribution. The FI matrix about $\vec{\phi}$ given this Gaussian distribution is presented in Eq. (21) in the main text. We write it here as

$$I = D^{\dagger}\Sigma^{-1}D, \quad \text{(A2)}$$

where

$$D = \begin{pmatrix} \partial_{\phi_1}\mu_{1,2} & \partial_{\phi_2}\mu_{1,2} & \cdots & \partial_{\phi_N}\mu_{1,2} \\ \vdots & \vdots & \vdots & \vdots \\ \partial_{\phi_1}\mu_{N-1,N} & \partial_{\phi_2}\mu_{N-1,N} & \cdots & \partial_{\phi_N}\mu_{N-1,N} \end{pmatrix}. \quad \text{(A3)}$$

Hence, we need to calculate $\{\mu_{i,j}\}_{i,j>i}$ and Σ in order to get the FI matrix. Let us first assume only correlated dephasing (no uncorrelated dephasing). For the mean values, we have

$$\mu_{i,j} = 2\left[\frac{1}{2\pi}\int_0^{2\pi} \cos^2\left(\frac{1}{2}(\phi_i+\varphi_m)\right)\cos^2\left(\frac{1}{2}(\phi_j+\varphi_m)\right) + \sin^2\left(\frac{1}{2}(\phi_i+\varphi_m)\right)\sin^2\left(\frac{1}{2}(\phi_j+\varphi_m)\right)d\varphi_m\right] - 1 = \frac{1}{2}\cos(\phi_i-\phi_j). \tag{A4}$$

Let us now calculate Σ. The diagonal terms of Σ read

$$\Sigma_{(i,j),(i,j)} = \langle q_i^2 q_j^2\rangle - \langle q_i q_j\rangle^2 = 1 - \frac{1}{4}\cos^2(\phi_i-\phi_j) = \frac{7}{8} - \frac{\cos(2(\phi_i-\phi_j))}{8}. \tag{A5}$$

Regarding the nondiagonal terms, let us begin with nonoverlapping pairs $(i,j),(k,n)$:

$$\langle q_i q_j q_k q_n\rangle = \frac{1}{8}\cos(\phi_i+\phi_j-\phi_k-\phi_n) + \frac{1}{4}\cos(\phi_i-\phi_j)\cos(\phi_k-\phi_n),$$
$$\langle q_i q_j\rangle\langle q_k q_n\rangle = \frac{1}{4}\cos(\phi_i-\phi_j)\cos(\phi_k-\phi_n).$$

Hence,

$$\Sigma_{(i,j),(k,n)} = \frac{1}{8}\cos(\phi_i+\phi_j-\phi_k-\phi_n). \tag{A6}$$

For overlapping pairs, such as $(i,j),(i,n)$, we have

$$\Sigma_{(i,j),(i,n)} = \langle q_i^2 q_j q_n\rangle - \langle q_i q_j\rangle\langle q_i q_n\rangle = \langle q_j q_n\rangle - \langle q_j q_i\rangle\langle q_i q_n\rangle = \frac{3}{8}\cos(\phi_j-\phi_n) - \frac{1}{8}\cos(\phi_j+\phi_n-2\phi_i). \tag{A7}$$

The derivatives matrix D is

$$D_{(i,j),m} = \begin{cases} -\frac{1}{2}\sin(\phi_i-\phi_j) & m=i, \\ \frac{1}{2}\sin(\phi_i-\phi_j) & m=j, \\ 0 & m\neq i,j. \end{cases} \tag{A8}$$

Inserting Eqs. (A4)–(A7) into Eq. (A2), we can perform exact numerical calculations of the FI.

Given an uncorrelated dephasing in addition to the correlated dephasing, the probabilities $p_\pm$ of observing outcomes $q_i = \pm 1$ are modified to $p_\pm = \frac{1}{2}[1 \pm C_0 \sin(\phi_i+\varphi_m)]$, i.e., a finite contrast of $0 \le C_0 \le 1$. It can be immediately observed that $\mu_{i,j} = \frac{1}{2}C_0^2\cos(\phi_i-\phi_j)$. The covariance matrix is modified as follows:

$$\Sigma_{(i,j),(i,j)} = \left(1-\frac{C_0^4}{8}\right) - C_0^4\frac{\cos(2(\phi_i-\phi_j))}{8},$$
$$\Sigma_{(i,j),(k,n)} = \frac{1}{8}C_0^4\cos(\phi_i+\phi_j-\phi_k-\phi_n),$$
$$\Sigma_{(i,j),(i,n)} = \left(\frac{1}{2}C_0^2 - \frac{1}{8}C_0^4\right)\cos(\phi_j-\phi_n) - \frac{1}{8}C_0^4\cos(\phi_j+\phi_n-2\phi_i).$$

Let us analyze the uncertainty using pair correlations as $N\to\infty$. The behavior in the limit of large N is presented in Fig. 10. It can be observed that for $C_0 = 1$ this uncertainty does not converge to the noiseless precision bound of $\sqrt{2/M}$ but approximately to $\sqrt{3/M}$.

The limit of $\sqrt{3/M}$ can be derived analytically, assuming that the phases are distributed evenly in $k\pi(k\in\mathbb{Z})$. To obtain this result, we use the following approximation of the variance:

$$\mathrm{var}(\phi_1-\phi_2) = u_{1,2}^\dagger(D^\dagger\Sigma^{-1}D)^{-1}u_{1,2} \approx \frac{||u_{1,2}||^4}{||Du_{1,2}||^4}(Du_{1,2})^\dagger\Sigma(Du_{1,2}),$$

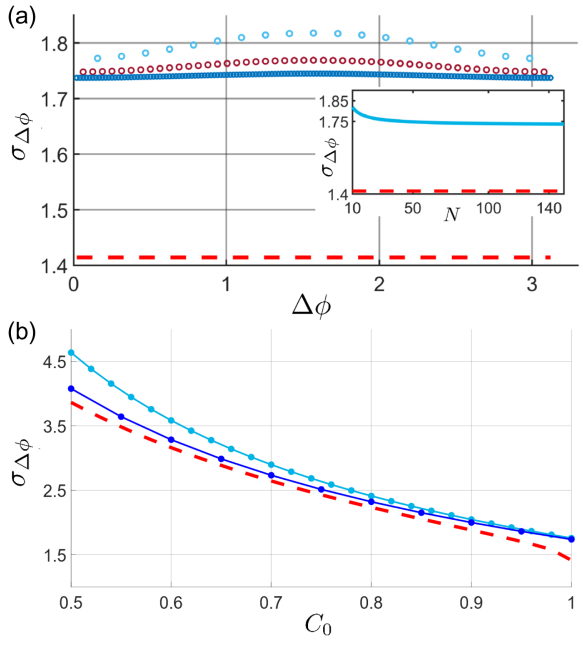

FIG. 10. Sensitivity (per measurement) with pair correlations compared to precision bounds (numerical analysis). (a) Uncertainty in estimating $\Delta\phi$ using all pair correlations as a function of $\Delta\phi$ for different numbers of ions. The dashed red line is the noiseless precision bound, pair correlations of $N = 20$, 50, and 150 correspond to light blue (top), red (middle), and dark blue (bottom) points, respectively. Inset: standard deviation averaged over all phases as a function of N; the top (bottom) lines correspond to pair correlations (noiseless precision bound). (b) Uncertainty as a function of the contrast C_0. The red dashed line corresponds to the finite contrast precision bound. Light blue (top) and blue (bottom) points correspond to pair correlations for $N = 30$ and 120, respectively.

where $u_{1,2}$ is the vector that corresponds to $\phi_2-\phi_1$, i.e., $(-1,1,0,\ldots,0)$. This approximation is obtained by using a Cauchy-Schwarz inequality twice: $v^\dagger M^{-1}v \geq (\|v\|^4/v^\dagger Mv)$, and it can be understood as a single parameter estimation bound where the derivative of the mean is $(1/\|u_{1,2}\|^2)Du_{1,2}$ and the variance is $(1/\|Du_{1,2}\|^4)(Du_{1,2})^\dagger\Sigma(Du_{1,2})$. We now calculate this approximation to show that in the limit of large N it converges to 3.

Clearly, $\|u_{12}\|^4=4$, and $\|Du_{1,2}\|^4 \approx (2\sum_{k=1}^{N}\frac{1}{4}\times \sin(2k\phi)^2)^2 \approx (N^2/16)$. We now need to calculate $(Du_{1,2})^\dagger\Sigma(Du_{1,2})$: Note that, since the denominator goes as N^2, we can omit in the calculation of this term any contributions that are smaller than N^2. Since $Du_{1,2}$ is a real vector, this term is given by the sum (summation convention is used) $(Du_{1,2})_{(i,j)}\Sigma_{(i,j)(k,n)}(Du_{1,2})_{(k,n)}$. We can neglect the N terms of identical pairs. From overlapping pairs $(i,j),(i,n)$, the contribution is

$$\begin{aligned}
&2\langle q_i^2 q_j q_n\rangle (Du_{1,2})_{(i,j)}(Du_{1,2})_{(i,n)}\\
&\quad\approx \frac{2}{8}\cos(\phi_j-\phi_n)\sin(\phi_1-\phi_j)\sin(\phi_1-\phi_n)\\
&\qquad+\frac{2}{8}\cos(\phi_j-\phi_n)\sin(\phi_2-\phi_j)\sin(\phi_2-\phi_n)\\
&\quad\approx N^2/16.
\end{aligned}$$

The contribution from the nonoverlapping pairs is

$$\begin{aligned}
&2\langle q_i q_j q_k q_n\rangle (Du_{1,2})_{(i,j)}(Du_{1,2})_{(k,n)}\\
&\approx -\frac{2}{8}\cos(\phi_1+\phi_j-\phi_2-\phi_n)\frac{1}{2}\sin(\phi_1-\phi_j)\frac{1}{2}\sin(\phi_2-\phi_n)\\
&\approx -N^2/48.
\end{aligned}$$

Hence, $(Du_{1,2})^\dagger\Sigma(Du_{1,2}) \approx (N^2/16)(1-\frac{1}{4}) = (N^2/16)\frac{3}{4}$. Therefore, altogether,

$$\frac{\|u_{1,2}\|^4}{\|Du_{1,2}\|^4}(Du_{1,2})^\dagger\Sigma(Du_{1,2}) \approx 3, \tag{A9}$$

which matches the numerical results.

For general contrast C_0, these expressions are modified to

$$\begin{aligned}
\|Du_{1,2}\|^4 &\approx \frac{N^2}{16}C_0^8,\\
2\langle q_i^2 q_j q_n\rangle (Du_{1,2})_{(i,j)}(Du_{1,2})_{(i,n)} &\approx C_0^8 N^2/16,\\
2\langle q_i q_j q_k q_n\rangle (Du_{1,2})_{(i,j)}(Du_{1,2})_{(k,n)} &\approx -C_0^6 N^2/48.
\end{aligned}$$

Hence, we obtain that for a general contrast $\mathrm{var}(\phi_1-\phi_2)$ from pair correlations converges to $\approx(4-C_0^2/C_0^2)$. This implies that as C_0 becomes smaller the uncertainty using pair correlations converges to the finite contrast bound of the variance $2/1-\sqrt{1-C_0^2}$. The reason for this convergence is that the Fisher information obtained from higher moments goes with higher powers of C_0; in general, the Fisher information obtained from the $2k$th moments goes as C_0^{2k}, and, thus, the contribution from the higher moment gets smaller for smaller C_0. In fact, the FI with pair correlations coincides with the finite contrast bound up to a second order in C_0^2: $2/1-\sqrt{1-C_0^2} = [4-C_0^2+\mathcal{O}(C_0^4)/C_0^2]$. This raises a natural question: Is the variance with all $m\leq k$ particle correlations equal to

$$\frac{2}{C_0^2}+\frac{2}{C_0^2}\left(1-\sum_{l=1}^{k}\frac{2}{l}\binom{2l-2}{l-1}\left(\frac{C_0^2}{4}\right)^l\right)?$$

We leave it as an open question (and conjecture), as we do not have a proof to this.

2. N-qubit correlations

The information about the phase differences when taking all correlations into account is the information contained in the full distribution averaged over the random phase:

$$P(\mathbf{q}) = \frac{2^{-N}}{2\pi}\int_0^{2\pi} d\varphi \prod_{i=1}^{N}[1+q_i\sin(\phi_i+\varphi)]. \tag{A10}$$

Hence, the precision bound is given by the FI matrix about ϕ with this distribution. Since the FI matrix involves summation over all 2^N possible $\mathbf{q}$ vectors, $I_{i,j}=\sum_{\mathbf{q}}[(\partial_{\phi_i}p(\mathbf{q}))(\partial_{\phi_j}p(\mathbf{q}))/p(\mathbf{q})]$, an exact calculation becomes intractable for large N. Hence, to make an efficient calculation of the FI, we use the fact that $I_{i,j}=\langle(\partial_{\phi_i}p)(\partial_{\phi_j}p)/p^2\rangle = \langle\partial_{\phi_i}\ln(p)\partial_{\phi_j}\ln(p)\rangle$. This allows us to make a Monte Carlo calculation of the FI matrix by sampling $\partial_{\phi_i}\ln(p)\partial_{\phi_j}\ln(p)$. Simulation results are shown in Fig. 11 for the case of evenly distributed single-qubit phases, $\phi_j=2\pi j/N$.

APPENDIX B: NUMERICAL SIMULATIONS

1. Estimating the phases with pair correlations: Maximum-likelihood and least-squares estimation

We calculate precision bounds of the phases given the pair correlations; in this part, we discuss estimation methods using pair correlations and the saturability of these precision limits. We compare between two estimation methods: simple least-squares estimation, i.e., minimizing $\mathbf{V}^\dagger\mathbf{V}$, where $\mathbf{V}=\{(1/M)\sum_{m=1}^{M}q_{i,m}q_{j,m}-\mu_{i,j}\}_{i,j}$, and maximum-likelihood estimation. Note that since the relevant distribution [Eq. (A1)] is Gaussian, the maximum-likelihood estimation becomes a weighted least-squares estimation [63]:

$$\max_{\phi}\mathcal{L}(\mathbf{V}|\phi) = \min_{\phi}\mathbf{V}^\dagger\Sigma^{-1}\mathbf{V}.$$

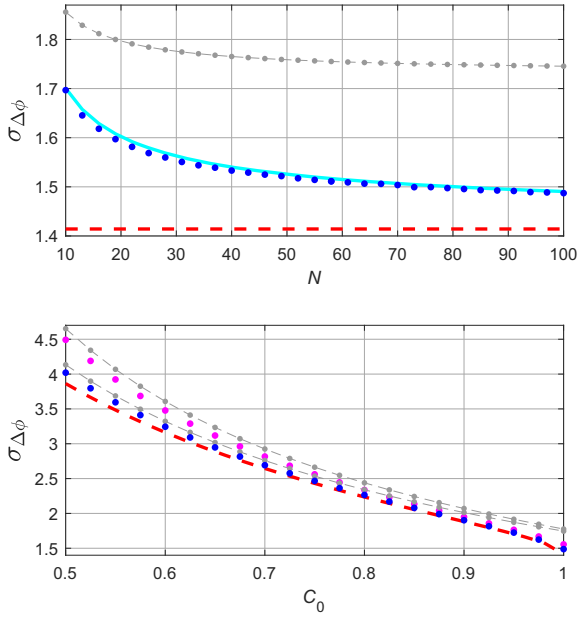

FIG. 11. Uncertainty with N-qubit correlations, pair correlations, and precision limits (all values are per measurement). (a) Precision bounds as a function of N: The gray (upper) curve and blue dots correspond to pair correlations and N-qubit correlations, respectively. The light blue curve corresponds to the analytical approximation, and the red dashed line is the fundamental noiseless limit of $\sqrt{2}$. (b) Precision bounds as a function of C_0: Pink dots and the gray (upper) curve correspond to all N correlations and pair correlations, respectively, for $N = 30$. The same for blue dots and the gray lower curve for $N = 100$. The red dashed line corresponds to the finite contrast precision bound.

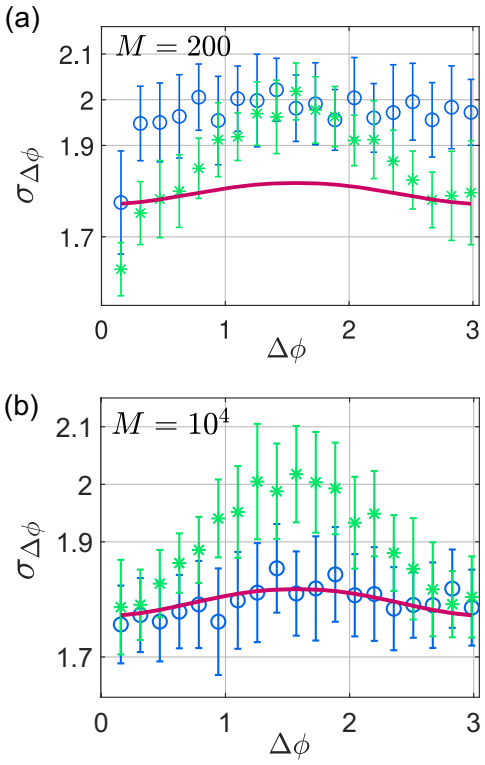

FIG. 12. Phase estimation errors using simple least-squares and maximum-likelihood estimation for 200 and 10^4 samples and 20 qubits (data from numerical simulation). Green lines and blue lines correspond to the distribution of the estimation errors with simple least squares and maximum likelihood, respectively. The green circles and blue diamonds correspond to the average estimation error. The red solid line correspond to the Cramer-Rao limit. (a) For 200 samples, the estimation errors are above the limit, and simple least squares performs better than maximum likelihood. This behavior is due to the small number of samples. (b) For 10^4 samples, the behavior matches the expectations: Maximum likelihood coincides with the Fisher information and outperforms simple least squares.

The difference between the two estimation methods is, thus, rooted in the weights given by the inverse of the covariance matrix, Σ^{-1}. The maximum likelihood is, in general, asymptotically efficient, i.e., saturates the Fisher information, whereas the simple least square is more straightforward, as it does not require evaluation of the covariance matrix.

A comparison of both approaches is presented in Fig. 12. It can be observed that for a large number of samples (here, $M = 10^4$) the maximum likelihood indeed saturates the FI, while the simple least-squares method does not saturate it. Interestingly, for a smaller number of samples (here, $M = 200$), maximum likelihood does not saturate the FI and a simple least-squares approximation outperforms it. In fact, for some phases, simple least squares even outperforms the FI (due to its bias for small number of samples).

2. Estimating the phases from N-qubit correlations

A maximum-likelihood estimation of the phases by analysis of N-qubit correlations via Eq. (8) satisfies the FI-based bound in the limit of infinite sample size. We carry out numerical simulations of the phase estimation process to investigate the influence of a finite number of samples on the phase uncertainties. The simulations show the uncertainty increasing over the FI bound with decreasing sample size M; however, the effect is not very pronounced: In simulations with 20 and 100 qubits, we observe an increase by about 10% for $M = 50$ and by about 1% for $M = 500$.

APPENDIX C: IMPROVING THE PRECISION WITH ENTANGLED STATES AND NONLOCAL MEASUREMENTS

Let us inquire about the optimality of our scheme by asking the following question: What is the optimal precision optimized over all possible initial states and measurement strategies? The figure of merit is $1/\binom{N}{2}\sum_{j>k}\mathrm{Var}(\phi_j - \phi_k)$. We first show that the noiseless precision bound can be obtained by modifying the measurement basis to a nonlocal

one. In a second step, we consider also entangled input states and find an optimal initial state for this sensing task.

Let us introduce the following notation for this part: The state $|\vec{z}\rangle$ is the product state $|z_1\rangle|z_2\rangle\ldots|z_N\rangle$, where $|z_i\rangle$ is an eigenstate of Z_i with eigenvalue $z_i \in \{\pm 1\}$. A different notation to the same state would be $|\vec{q}\rangle$, where $q_i = (1 - z_i/2)$, and, thus, $z_i = 1 \to q_i = 0$, $z_i = -1 \to q_i = 1$.

1. Improving precision with nonlocal measurements

Let us first write the quantum state after the time evolution. The initial state is a pure product state: $|+\rangle^N$, with $|+\rangle = (1/\sqrt{2})(|0\rangle + |1\rangle)$ (an eigenstate of X with eigenvalue $+1$). After a free evolution, the state evolves into the state of Eq. (1) with phases $\phi_{im} = \phi_i + \varphi_m$. φ_m is a random phase that is distributed uniformly in $[0, 2\pi]$. This random phase induces a correlated dephasing; i.e., the final state, after averaging out φ_m, becomes a mixture of Dicke states:

$$\rho_f = \bigoplus_{j=0}^{N} \rho_j,$$

where ρ_j is a Dicke state with j excitation:

$$\rho_j = \frac{\binom{N}{j}}{2^N} |\psi_j\rangle\langle\psi_j|, \qquad |\psi_j\rangle = \frac{1}{\sqrt{\binom{N}{j}}} \sum_{\vec{q}\cdot\sum_k q_k = j} e^{i\vec{\phi}\cdot\vec{q}} |\vec{q}\rangle.$$

Given $\rho_f(\vec{\phi})$, the fundamental precision limit is set by the quantum Fisher information matrix (QFIM) about the parameters $\phi_1, \phi_2, \ldots, \phi_N$; this is the Fisher information matrix optimized over all possible measurement strategies. Hence, the covariance matrix of the estimators, Σ, satisfies

$$\Sigma \geq I^{-1},$$

where I is the QFIM, and, thus, for any j, k,

$$\mathrm{var}(\phi_j - \phi_k) \geq u^{\dagger}_{(j,k)} I^{-1} u_{(j,k)},$$

where $u_{(j,k)}$ is the parameter vector that corresponds to $\phi_j - \phi_k$.

For a general mixed state ρ, given its spectral decomposition $\rho = \sum_k p_k |k\rangle\langle k|$, the QFIM is given by [49]

$$I_{i,j} = 2 \sum_{k,l} \frac{\left(\frac{\partial\rho}{\partial\phi_i}\right)_{k,l} \left(\frac{\partial\rho}{\partial\phi_j}\right)_{l,k}}{(p_l + p_k)},$$

where $\{p_k\}_k$ are the eigenvalues of ρ and the matrix elements $(\bullet)_{k,l} = \langle k| \bullet |l\rangle$ are with respect to the eigenbasis of ρ.

For pure states, this expression is reduced to

$$I_{i,j} = 4(\langle \partial_{\phi_i}\psi | \partial_{\phi_j}\psi\rangle - \langle \partial_{\phi_i}\psi|\psi\rangle\langle\psi|\partial_{\phi_j}\psi\rangle). \quad \text{(C1)}$$

Let us calculate the QFIM of our ρ_f, which we denote as I. It can be observed that in this special case I is a weighted sum of the QFIM of each $|\psi_j\rangle$ [64]:

$$I = \sum_{j=0}^{N} \frac{\binom{N}{j}}{2^N} I^{(j)}, \quad \text{(C2)}$$

where $I^{(j)}$ is the QFIM of $|\psi_j\rangle$. For every $|\psi_j\rangle$, we have $\partial_{\phi_i}|\psi_j\rangle = -i\frac{1}{2}(Z_i + \mathbb{I})|\psi_j\rangle$; inserting this into Eq. (C1), we get that the QFIM of each $|\psi_j\rangle$ is

$$I^{(j)}_{k,l} = (\langle\psi_j|Z_k Z_l|\psi_j\rangle - \langle\psi_j|Z_k|\psi_j\rangle\langle\psi_j|Z_l|\psi_j\rangle).$$

Now $|\psi_j\rangle$ is a symmetric superposition of all states with j excitations; from symmetry, we get

$$\langle Z_k\rangle = \frac{1}{N}(N - j - j) = \frac{N - 2j}{N}$$

and for $k \neq l$

$$\langle Z_k Z_l\rangle = \frac{(N-2j)^2 - N}{N(N-1)}.$$

Hence, all the nondiagonal terms of $I^{(j)}$ are

$$I^{(j)}_{k,l} = \frac{(N-2j)^2 - N}{N(N-1)} - \frac{(N-2j)^2}{N^2} = \frac{4j(j-N)}{N^2(N-1)}.$$

The diagonal terms of $I^{(j)}$ read

$$I^{(j)}_{k,k} = 1 - \left(\frac{N-2j}{N}\right)^2 = \frac{4j(N-j)}{N^2}.$$

Inserting these terms into Eq. (C2), we get that I reads

$$I = \begin{cases} \sum_{j=0}^{N} \frac{\binom{N}{j}}{2^N} \frac{4j(j-N)}{N^2(N-1)} = -\frac{1}{N}, & k \neq l, \\ \sum_{j=0}^{N} \frac{\binom{N}{j}}{2^N} \frac{4j(N-j)}{N^2} = \frac{N-1}{N}, & k = l. \end{cases}$$

It is now simple to see that for any $k \neq m$ the vector that corresponds to $\phi_k - \phi_m$ is an eigenvector of I with an eigenvalue of 1. The variance per measurement is, thus,

$$\mathrm{var}(\phi_k - \phi_m) = 2,$$

and this is exactly the noiseless precision bound. Since the strong commutativity condition is satisfied (all Hamiltonian

terms commute with each other), we know that there exists a basis that saturates this QFI [65]. This implies that there exists a measurement strategy such that the noiseless precision bound is obtained.

As a simple example, we examine the case of two qubits. The density matrix for two qubits reads

$$\rho_f = \frac{1}{4}(|11\rangle\langle 11| + |00\rangle\langle 00|) + \frac{1}{2}|\psi_1\rangle\langle\psi_1|,$$

with $|\psi_1\rangle = (1/\sqrt{2})(|01\rangle + e^{i(\phi_1-\phi_2)}|10\rangle)$. Measuring the local X basis, we project onto the states $|\vec{x}\rangle = |x_1\rangle|x_2\rangle\ldots|x_N\rangle$ where $|x_i\rangle$ is an eigenstate of X_i with eigenvalues $x_i \in \{\pm 1\}$ and obtain the probabilities

$$\text{even } \vec{x}\text{: } \frac{1}{8} + \frac{1}{4}\cos\left(\frac{\phi_1-\phi_2}{2}\right)^2,$$
$$\text{odd } \vec{x}\text{: } \frac{1}{8} + \frac{1}{4}\sin\left(\frac{\phi_1-\phi_2}{2}\right)^2,$$

where $\vec{x}$ odd (even) stands for $\#(x_i = -1)$ odd (even). This leads to

$$\text{var}(\phi_2 - \phi_1) = \frac{4 - \cos\,(\phi_1-\phi_2)^2}{\sin\,(\phi_1-\phi_2)^2} \geq 4;$$

clearly, this is exactly the variance with a single-pair correlation and, thus, does not saturate the QFI. It can be observed that optimizing over all local measurement bases is equivalent to optimizing over ϕ_1, ϕ_2, and, thus, no local measurement saturates the QFI. There exists, however, a nonlocal measurement strategy that saturates the QFI: Consider first measuring $Z_1 + Z_2$ and then measuring the local X basis. With probability $1/2$ we get $|00\rangle, |11\rangle$ in the first measurement and, thus, no information, and with probability $1/2$ we collapse into $|\psi_1\rangle$ which yields a Fisher information of 1. Therefore, the total Fisher information is

$$\frac{1}{2}\cdot 0 + \frac{1}{2}\cdot 1 = \frac{1}{2} \to \text{var}(\phi_2 - \phi_1) = 2;$$

hence, the bound is saturated.

A general optimal measurement strategy would be (i) first measure $\sum_i Z_i$ (this measurement collapses the density matrix into one of the Dicke states $|\psi_j\rangle$) and (ii) measure the Dicke state $|\psi_j\rangle$ in its optimal measurement basis.

The optimal measurement basis of $|\psi_j\rangle$ can be written implicitly as proven in Ref. [65]: Projecting into a (Gram-Schmidt) orthogonalization of $\{|\psi_j\rangle, |\partial_{\phi_k}\psi_j\rangle\}_{\phi_k}$ would be optimal. For example, for $N = 3$, given $|\psi_1\rangle = (1/\sqrt{3})(|011\rangle + |101\rangle + |110\rangle)$ (we can assume for convenience $\phi_1 = \phi_2 = \phi_3 = 0$; this can be achieved adaptively by local operations), an optimal measurement basis would be

$$\frac{1}{\sqrt{3}}(|011\rangle + |101\rangle + |110\rangle),$$
$$\frac{1}{\sqrt{6}}(-2|011\rangle + |101\rangle + |110\rangle),$$
$$\frac{1}{\sqrt{2}}(|101\rangle - |110\rangle).$$

The construction for $|\psi_2\rangle$ is equivalent.

2. Optimal initial states

We show that the average variance of phase difference $1/\binom{N}{2}\sum_{j>k}\text{Var}(\phi_j - \phi_k)$ is lower bounded by $2(N - 1/N)$, and we find several initialization strategies, all of which involve entanglement, that saturate this bound. In particular, the symmetric Dicke state

$$|\psi\rangle = \frac{1}{\sqrt{\binom{N}{N/2}}}\sum_{\vec{z} \text{ with } \sum_i z_i = 0} |\vec{z}\rangle$$

and any other state that is an equal superposition of states with $\sum_i z_i = 0$ saturate this optimal precision. Another strategy is a probabilistic initialization from an ensemble of products of antiparallel Bell pairs. It can be shown that all optimal strategies involve eigenstates of $\sum_i Z_i$ with eigenvalue 0. Since these states are robust against correlated dephasing, this optimal precision is achieved irrespective of whether there is correlated dephasing or not. In the following derivation, we use techniques similar to those used in Ref. [40].

We denote the final and initial states as $|\psi_f\rangle$ and $|\psi\rangle$, respectively, where $|\psi_f\rangle = U|\psi\rangle$, with $U = \exp(-i\frac{1}{2}\vec{\phi}\cdot\vec{Z})$. Since $|\partial_{\phi_j}\psi_f\rangle = -(i/2)Z_j U|\psi\rangle$, the QFIM of $|\psi_f\rangle$ reads

$$I_{i,j} = (\langle\psi|Z_i Z_j|\psi\rangle - \langle\psi|Z_i|\psi\rangle\langle\psi|Z_j|\psi\rangle).$$

Using the QFIM, we prove that the optimal achievable variance $1/\binom{N}{2}\sum_{j>k}\text{Var}(\phi_j - \phi_k)$ is $2(N - 1/N)$.

Proof. By definition of QFIM,

$$\text{var}(\phi_j - \phi_k) \geq u^\dagger_{(j,k)} I^{-1} u_{(j,k)}.$$

The Cauchy-Schwarz inequality $(u^\dagger I^{-1} u)(u^\dagger I u) \geq |u^\dagger\sqrt{I^{-1}}\sqrt{I}u|^2$ implies

$$\left(u^\dagger_{(j,k)} I^{-1} u_{j,k}\right) \geq \frac{||u_{(j,k)}||^4}{\left(u^\dagger_{(j,k)} I u_{(j,k)}\right)}.$$

Hence,

$$\mathrm{var}(\phi_j-\phi_k)\geq\frac{||u_{(j,k)}||^4}{\left(u^\dagger_{(j,k)}Iu_{(j,k)}\right)}=\frac{4}{I_{jj}+I_{kk}-2I_{jk}}\geq\frac{2}{(1-\langle Z_jZ_k\rangle)}.$$

Therefore, we seek to lower bound $\sum_{j<k}[2/(1-\langle Z_jZ_k\rangle)]$. The minimal possible $\mathrm{var}(\phi_j-\phi_k)$ is, therefore, obtained when $\langle Z_jZ_k\rangle=-1$; however, there is no state that satisfies $\langle Z_jZ_k\rangle=-1$ for all j and k. To lower bound $\sum_{j<k}[2/(1-\langle Z_jZ_k\rangle)]$, we use the Cauchy-Schwarz inequality:

$$2\left(\sum_{j<k}\frac{1}{(1-\langle Z_jZ_k\rangle)}\right)\left(\sum_{j<k}(1-\langle Z_jZ_k\rangle)\right)\geq 2\left(\sum_{j<k}1\right)^2=2\sum_{j<k}\binom{N}{2}.$$

The first inequality is due to

$$\left(\sum_i\frac{1}{x_i}\right)\left(\sum_i x_i\right)\geq\left(\sum_i\frac{1}{\sqrt{x_i}}\cdot\sqrt{x_i}\right)^2=\left(\sum_i 1\right)^2,$$

which is just the Cauchy-Schwarz inequality.

Hence,

$$\sum_{j<k}\mathrm{Var}(\phi_j-\phi_k)\geq 2\sum_{j<k}\frac{\binom{N}{2}}{\sum_{j<k}(1-\langle Z_jZ_k\rangle)}.$$

Note that $\langle\sum_i Z_i\rangle^2=2\sum_{j<k}\langle Z_jZ_k\rangle+N$; therefore, $2\sum_{j<k}\langle Z_jZ_k\rangle\geq -N$. Hence,

$$\sum_{j<k}\mathrm{Var}(\phi_j-\phi_k)\geq\sum_{j<k}\frac{4\binom{N}{2}}{2\binom{N}{2}+N}=2\sum_{j<k}\frac{N-1}{N}.$$

This basically proves that $1/\binom{N}{2}\sum_{j<k}\mathrm{Var}(\phi_j-\phi_k)\geq 2(N-1/N)$. To show that this lower bound is saturable, we need to find an initial state $|\psi\rangle$ for which all these inequalities are saturated, namely,

$$\sum_{j<k}u^\dagger_{(j,k)}I^{-1}u_{(j,k)}=2\sum_{j<k}\frac{N-1}{N},$$

where I is the QFIM given this $|\psi\rangle$. We observe that a necessary condition is $\langle Z_i\rangle=0$ and identical $\langle Z_jZ_k\rangle=-(1/N-1)$. Let us show that this is also a sufficient condition: Given that this condition is satisfied, the QFIM is

$$I_{i,j}=\begin{cases}1 & i=j,\\ -\frac{1}{N-1} & i\neq j.\end{cases}$$

It can be now observed that any $u_{(j,k)}$ is an eigenvector of this matrix with eigenvalue $N/N-1$ and, thus, for any j, k, $u^\dagger_{(j,k)}I^{-1}u_{(j,k)}=2(N-1/N)$.

Hence, any initial pure state that satisfies the conditions

$$\forall\, i\langle Z_i\rangle=0\quad\text{and}\quad\forall\, j,k\langle Z_jZ_k\rangle=-\frac{1}{N-1}\tag{C3}$$

saturates this QFIM. We can immediately observe that the symmetric Dicke state

$$|\psi\rangle=\frac{1}{\sqrt{\binom{N}{N/2}}}\sum_{\vec{z}\text{ with }\sum_i z_i=0}|\vec{z}\rangle$$

satisfies these conditions and, thus, saturates this bound. Other strategies exist, such as preparing a classical ensemble of products of antiparallel Bell states, and they are discussed later. For now, let us focus on the symmetric Dicke state.

To show that indeed $\mathrm{Var}(\phi_j-\phi_k)=2(N-1/N)$ can be achieved with $|\psi\rangle$, we need to find a readout strategy that achieves this bound, i.e., a measurement with a classical FI matrix that equals the QFIM. We show that local measurements in X saturate this optimal variance.

To show this, let us first write $|\psi_f\rangle$, the final probe state given the initial symmetric Dicke state:

$$|\psi_f\rangle=\frac{1}{\sqrt{\binom{N}{N/2}}}\sum_{\sum_i z_i=0,z_1=1}\left(e^{-i\frac{1}{2}\vec{\phi}\cdot\vec{z}}|\vec{z}\rangle+e^{i\frac{1}{2}\vec{\phi}\cdot\vec{z}}|-\vec{z}\rangle\right)\tag{C4}$$

$$=\frac{\sqrt{2}}{\sqrt{\binom{N}{N/2}}}\sum_{\sum_i z_i=0,z_1=1}\cos\left(\frac{1}{2}\vec{\phi}\cdot\vec{z}\right)|+_{\vec{z}}\rangle-i\sin\left(\frac{1}{2}\vec{\phi}\cdot\vec{z}\right)|-_{\vec{z}}\rangle,\tag{C5}$$

where $|\pm_{\vec{z}}\rangle=(1/\sqrt{2})(|\vec{z}\rangle\pm|-\vec{z}\rangle)$.

Let us now use Theorem 2 in Ref. [65]: Given a pure probe state $|\Psi(\vec{\phi})\rangle$, then a projective measurement that consists of rank 1 projectors $\{\Pi_k\}_k$ saturates the QFIM if and only if for every k and j

$$\mathrm{Im}(\langle\Psi|\Pi_k|\partial_{\phi_j}\Psi_\perp\rangle)=0,\tag{C6}$$

where $|\partial_{\phi_j}\Psi_\perp\rangle:=|\partial_{\phi_j}\Psi\rangle-|\Psi\rangle\langle\Psi|\partial_{\phi_j}\Psi\rangle$; i.e., it is the projection of $|\partial_{\phi_j}\Psi\rangle$ onto the orthogonal subspace of

$|\Psi\rangle$. The full proof of this theorem is presented in Ref. [65]. Let us briefly explain the intuition behind this theorem: Given $|\Psi\rangle$, the probability of detecting the kth result is $p_k = \langle\Psi|\Pi_k|\Psi\rangle$. The derivative of this probability with respect to ϕ_j is $\partial_{\phi_j} p_k = 2\mathrm{Re}\langle\Psi|\Pi_k|\partial_{\phi_j}\Psi\rangle$. The parallel part of $|\partial_{\phi_j}\Psi\rangle$, i.e., $|\partial_{\phi_j}\Psi_\parallel\rangle \coloneqq \langle\Psi|\partial_{\phi_j}\Psi\rangle|\Psi\rangle$, does not contribute to the derivative, because $\mathrm{Re}\langle\Psi|\Pi_k|\partial_{\phi_j}\Psi_\parallel\rangle = 0$. The derivative can, therefore, be written as $\partial_{\phi_j} p_k = 2\mathrm{Re}\langle\Psi|\Pi_k|\partial_{\phi_j}\Psi_\perp\rangle$. Hence, if $\mathrm{Im}\langle\Psi|\Pi_k|\partial_{\phi_j}\Psi_\perp\rangle \neq 0$, then some of the information about ϕ_j is being lost when measuring in this basis; i.e., a change ϕ_j is being translated to a change in the phase and not the probability. If $\mathrm{Im}\langle\Psi|\Pi_k|\partial_{\phi_j}\Psi_\perp\rangle = 0$ for every j and k, then no information about $\vec{\phi}$ is lost, and, thus, the QFIM is being saturated. We remark that this intuitive argument is correct only for pure states.

Let us apply this theorem to our case: We need to show that the condition of Eq. (C6) is satisfied for our $|\psi_f\rangle$ and local X measurements. The rank 1 projectors in our case are, thus, $\{\Pi_{\vec{x}} = |\vec{x}\rangle\langle\vec{x}|\}_{\vec{x}}$. Hence, we need to show that, for every $\vec{x}$, $\mathrm{Im}(\langle\psi_f|\Pi_{\vec{x}}|\partial_{\phi_j}\psi_{f\perp}\rangle) = 0$.

Let us use the following identity:

$$\langle\vec{x}|\frac{1}{\sqrt{2}}(|\vec{z}\rangle + |-\vec{z}\rangle) = \frac{1}{\sqrt{2^{N+1}}}\left[(-1)^{\vec{q}_{\vec{x}}\cdot\vec{q}_{\vec{z}}} + (-1)^{\vec{q}_{\vec{x}}\cdot\vec{q}_{-\vec{z}}}\right],$$

with $(\vec{q}_{\vec{z}})_i = \frac{1}{2}(1 - z_i)$ and $\vec{q}_{\vec{x}}$ and analogously $(\vec{q}_{\vec{x}})_i = \frac{1}{2}(1 - x_i)$. Note that $\vec{q}_{\vec{x}}\cdot\vec{q}_{\vec{z}} + \vec{q}_{\vec{x}}\cdot\vec{q}_{-\vec{z}} = \#(x_i = -1)$; hence, if $\#(x_i = -1)$ is even, then $(-1)^{\vec{q}_{\vec{x}}\cdot\vec{q}_{\vec{z}}} = (-1)^{\vec{q}_{\vec{x}}\cdot\vec{q}_{-\vec{z}}}$, and if it is odd, $(-1)^{\vec{q}_{\vec{x}}\cdot\vec{q}_{\vec{z}}} = -(-1)^{\vec{q}_{\vec{x}}\cdot\vec{q}_{-\vec{z}}}$. Therefore,

$$\langle\vec{x}|\frac{1}{\sqrt{2}}(|\vec{z}\rangle + |-\vec{z}\rangle) = \begin{cases} 0 & \vec{x}\text{ odd} \\ \pm\frac{1}{\sqrt{2^N}} & \vec{x}\text{ even} \end{cases} \tag{C7}$$

and

$$\langle\vec{x}|\frac{1}{\sqrt{2}}(|\vec{z}\rangle - |-\vec{z}\rangle) = \begin{cases} \pm\frac{1}{\sqrt{2^N}} & \vec{x}\text{ odd} \\ 0 & \vec{x}\text{ even.} \end{cases} \tag{C8}$$

Inserting Eqs. (C7) and (C8) into Eq. (C5), we can observe that

$$\langle\vec{x}|\psi_f\rangle = \frac{1}{\sqrt{2^{N-1}\binom{N}{N/2}}}\cdot\begin{cases} (-i)\sum\limits_{\sum_i z_i = 0, z_1 = 1} (-1)^{\sum_i (\vec{q}_{\vec{x}})_i (\vec{q}_{\vec{z}})_i}\sin\left(\frac{1}{2}\vec{\phi}\cdot\vec{z}\right) & \vec{x}\text{ odd} \\ \sum\limits_{\sum_i z_i = 0, z_1 = 1} (-1)^{\sum_i (\vec{q}_{\vec{x}})_i (\vec{q}_{\vec{z}})_i}\cos\left(\frac{1}{2}\vec{\phi}\cdot\vec{z}\right) & \vec{x}\text{ even.} \end{cases}$$

Therefore, for any value of $\vec{\phi}$, $\langle\vec{x}|\psi_f\rangle$ is either real (for even $\vec{x}$) or imaginary (for odd $\vec{x}$). Similarly, it is simple to observe that $\langle\vec{x}|\partial_{\phi_j}\psi_{f\perp}\rangle$ is real (imaginary) for even $\vec{x}$ (odd $\vec{x}$). To sum up,

$$\begin{aligned} &\vec{x}\text{ odd}\colon \langle\vec{x}|\psi_f\rangle, \langle\vec{x}|\partial_{\phi_j}\psi_{f\perp}\rangle \text{ imaginary} \\ &\qquad\Rightarrow \langle\psi_f|\Pi_{\vec{x}}|\partial_{\phi_j}\psi_{f\perp}\rangle \text{ real}, \\ &\vec{x}\text{ even}\colon \langle\vec{x}|\psi_f\rangle, \langle\vec{x}|\partial_{\phi_j}\psi_{f\perp}\rangle \text{ real} \Rightarrow \langle\psi_f|\Pi_{\vec{x}}|\partial_{\phi_j}\psi_{f\perp}\rangle \text{ real}. \end{aligned}$$

Hence, the condition in Eq. (C6) is satisfied, and, thus, the local X basis indeed saturates the QFIM.

We remark that another strategy to saturate the QFIM is to choose the initial state of each experiment from a classical ensemble of products of antiparallel Bell states. An antiparallel Bell state is defined as $|i,j\rangle = |0\rangle_i|1\rangle_j + |0\rangle_j|1\rangle_i$. A Bell-product state is then a product of $N/2$ such antiparallel Bell pairs; we denote any such state as $\prod_{k=1}^{N/2}|i_k, j_k\rangle$. It can be observed that the QFIM of any $\prod_{k=1}^{N/2}|i_k, j_k\rangle$ is $\mathbb{1} - \prod_k X_{i_k,j_k}$, where $X_{i_k,j_k} = |i_k\rangle\langle j_k| + \mathrm{H.c.}$ The total number of these states is $(N-1)(N-3)\ldots 1$, and the total number of states with a specific pair (i_k, j_k) is $(N-3)\ldots 1$. Hence, by sampling from a uniform distribution of these Bell-product states, the QFIM becomes the optimal one:

$$I_{i,j} = \begin{cases} -\frac{1}{N-1} & i \neq j \\ 1 & i = j \end{cases}.$$

This QFIM is saturated with local X (or Y) measurements, since these measurements saturate the QFIM of each Bell-product state individually.

Finally, we remark about the set of optimal initial pure states. These are the states that satisfy the conditions in Eq. (C3). The problem of finding optimal states (other than the symmetric Dicke state) is then basically solving a system of linear equations. First, observe that the conditions imply $\langle(\sum_i Z_i)^2\rangle = 0$; hence, any optimal pure state is an eigenstate of $\sum_i Z_i$ with eigenvalue 0. We can, therefore, write the states as $\sum_{\sum_i z_i = 0}\sqrt{p_{\vec{z}}}|\vec{z}\rangle$. The conditions then become a system of $\binom{N}{2} + N + 1$ linear equations for the distribution $\{p_{\vec{z}}\}$: $\forall\, j,k,i \sum_{\sum_i z_i = 0} p_{\vec{z}} z_j z_k = -\frac{1}{N-1}, \sum_{\sum_i z_i = 0} p_{\vec{z}} z_i = 0$, and $\sum_l p_l = 1$, with a constraint of $0 \leq p_l \leq 1$ for all l. The number of equations, $\binom{N}{2} + N + 1$, is smaller than the number of variables, $\binom{N}{N}/2$, which implies that there exist

solutions other than the symmetric one. Finding solutions that are simple to prepare, in terms of entanglement or circuit complexity, is an interesting problem, and we leave it as an open question.

APPENDIX D: GENERALIZATION TO ARBITRARY SPINS

We consider a generalization of our protocol to arbitrary spins. The motivation comes from experimental scenarios where there is no individual readout of the qubits but a global readout of ensembles of qubits. We consider N ensembles, the ensembles have different phases, and all of them have N_q qubits. Each ensemble, thus, corresponds to a single spin of size $J = (N_q/2)$. We analyze the performance of correlation spectroscopy in this case.

1. Pair correlations

Just as in the single-qubit case, we measure the $J_x = \frac{1}{2}\sum_{i=1}^{N_q}\sigma_i^x$ operator of each spin. Let us denote the outcomes of $2J_{x,k}$ measurement as Y_k, and for a specific realization of φ_m we denote it as $Y_k^{(\varphi_m)}$. $Y_k^{(\varphi_m)} + N_q/2$ has a binomial distribution: $(Y_k^{(\varphi_m)} + N_q/2) \sim \mathrm{Bi}(\cos^2(\phi_k + \varphi_m/2), N_q)$.

In single-pair correlations, we estimate $\phi_1 - \phi_2$ from $\langle Y_1 Y_2\rangle$, and the variance is, thus, $\langle Y_1^2 Y_2^2\rangle - \langle Y_1 Y_2\rangle^2$:

$$\begin{aligned}\langle Y_1 Y_2\rangle &= \int \langle Y_1^{(\varphi_m)}\rangle\langle Y_2^{(\varphi_m)}\rangle p(\varphi_m) d\varphi_m \\ &= \frac{N_q^2}{2\pi}\int \cos(\phi_1+\varphi_m)\cos(\phi_2+\varphi_m) d\varphi_m \\ &= \frac{N_q^2}{2}\cos(\phi_1-\phi_2).\end{aligned}$$

Let us calculate

$$\langle Y_1^2 Y_2^2\rangle = \int \langle Y_1^{(\varphi_m)2}\rangle\langle Y_2^{(\varphi_m)2}\rangle p(\varphi_m) d\varphi_m,$$

and we have $\langle Y_j^{(\varphi_m)2}\rangle = (N_q^2 + N_q/2) + (N_q^2 - N_q/2)\times \cos(2(\phi_j+\varphi_m))$, so

$$\begin{aligned}\langle Y_1^{(\varphi_m)2} Y_2^{(\varphi_m)2}\rangle = &\left[\frac{N_q^2+N_q}{2} + \frac{N_q^2-N_q}{2}\cos(2(\phi_1+\varphi_m))\right] \\ &\times\left[\frac{N_q^2+N_q}{2} + \frac{N_q^2-N_q}{2}\cos(2(\phi_2+\varphi_m))\right].\end{aligned}$$

After averaging over φ_m, we are left with

$$\langle Y_1^2 Y_2^2\rangle = \frac{1}{4}(N_q^2+N_q)^2 + \frac{1}{8}(N_q^2-N_q)^2\cos(2(\phi_1-\phi_2)).$$

The variance is, thus,

$$\begin{aligned}\langle Y_1^2 Y_2^2\rangle - \langle Y_1 Y_2\rangle^2 = &\frac{1}{8}N_q^2(N_q^2+4N_q+2) \\ &-\frac{1}{8}N_q^2(2N_q-1)\cos(2\Delta\phi),\end{aligned}$$

and the estimation variance, thus, reads

$$\begin{aligned}\sigma_{\Delta\phi}^2 &= \frac{\frac{1}{8}N_q^2(N_q^2+4N_q+2) - \frac{1}{8}N_q^2(2N_q-1)\cos(2\Delta\phi)}{\frac{N_q^4}{4}\sin(\Delta\phi)^2} \\ &= \frac{1}{2\sin(\Delta\phi)^2} + \frac{1}{N_q\sin(\Delta\phi)^2} + \frac{3/2}{N_q^2\sin(\Delta\phi)^2} \\ &\quad + \frac{2}{N_q} - \frac{1}{N_q^2}.\end{aligned}$$

The minimal variance (for every N_q) is, thus, obtained at $\Delta\phi = \pi/2$ for which $\sigma_{\Delta\phi}^2 = \frac{1}{2} + (3/N_q) + (1/2N_q^2)$. For general $\Delta\phi$, the large N_q limit is $1/2\sin(\Delta\phi)^2$. Hence, $\sigma_{\Delta\phi}^2$ does not drop as $1/N_q$. The reason for this behavior is that the noisy φ_m adds noise which does not go to 0 as $N_q \to \infty$. Mathematically, it is because

$$\langle Y_1 Y_2\rangle^2 \neq \int \langle Y_1^{(\varphi_m)} Y_2^{(\varphi_m)}\rangle^2 p(\varphi_m) \mathrm{d}\varphi_m.$$

This uncertainty is plotted in Fig. 13.

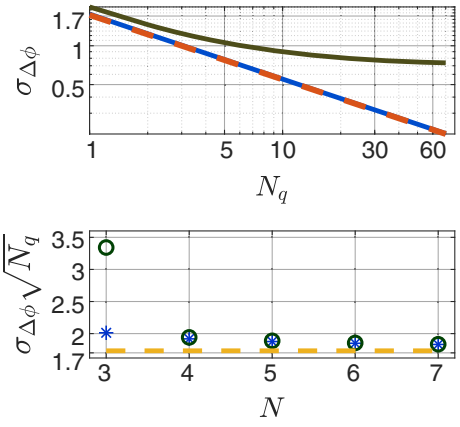

FIG. 13. Top: uncertainty with a single pair of spins correlations for (black line) compared to the uncertainty with multipair correlations (blue line). Both curves correspond to $\Delta\phi = \pi/2$, and $N = 50$. The uncertainty with multipair correlations coincides with $\sqrt{3/N_q}$ (dashed, orange line). Bottom: comparison between multipair correlations with and without qubit-resolved readout (blue stars and black circles, respectively). For large enough N, they coincide with the limit of $\sqrt{3/N_q}$ (dashed, orange line). In this illustration $N_q = 12$.

2. Multipair correlations

We generalize the calculation of the multipair correlations done in Appendix A to general spins. As in Appendix A, the pair correlations satisfy

$$\left\{\frac{1}{M}\sum_{m=1}^{M} Y_{i,m}Y_{j,m}\right\}_{i,j>i} \to \mathcal{N}\left(\{\mu_{i,j}\}_{i,j>i},\Sigma\right),$$

where $\mu_{i,j}=\langle Y_iY_j\rangle$ and Σ is the covariance matrix of Y_iY_j. The FI matrix is, thus, given by Eqs. (A2) and (A3), where the derivative matrix D now reads

$$D_{(i,j),m}=\begin{cases}-\frac{N_q^2}{2}\sin\left(\phi_i-\phi_j\right) & m=i\\ \frac{N_q^2}{2}\sin\left(\phi_i-\phi_j\right) & m=j\\ 0 & m\neq i,j.\end{cases} \tag{D1}$$

Let us, thus, calculate all the different terms of Σ. We already have

$$\langle Y_i^2Y_j^2\rangle-\langle Y_iY_j\rangle^2 = \frac{1}{8}N_q^2(N_q^2+4N_q+2)-\frac{1}{8}N_q^2(2N_q-1)\cos\left(2\Delta\phi\right).$$

$\langle Y_iY_jY_kY_n\rangle-\langle Y_iY_j\rangle\langle Y_kY_n\rangle$ is exactly the same as with qubits but with a factor of N_q^4:

$$\langle Y_iY_jY_kY_n\rangle-\langle Y_iY_j\rangle\langle Y_kY_n\rangle = \frac{N_q^4}{8}\cos\left(\phi_i+\phi_j-\phi_k-\phi_n\right).$$

$\langle Y_i^2Y_jY_n\rangle-\langle Y_iY_j\rangle\langle Y_iY_n\rangle$ is given by

$$\langle Y_i^2Y_jY_n\rangle = \frac{N_q^3}{8}[2(N_q-1)\cos\left(\phi_i-\phi_j\right)\cos\left(\phi_i-\phi_n\right) + (N_q+3)\cos\left(\phi_n-\phi_j\right)],$$

$$\langle Y_iY_j\rangle\langle Y_iY_n\rangle = \frac{N_q^4}{4}\cos\left(\phi_i-\phi_j\right)\cos\left(\phi_i-\phi_n\right).$$

Hence,

$$\langle Y_i^2Y_jY_n\rangle-\langle Y_iY_j\rangle\langle Y_iY_n\rangle = \frac{N_q^3}{8}(N_q+3)\cos\left(\phi_n-\phi_j\right) - \frac{N_q^3}{4}\cos\left(\phi_i-\phi_j\right)\cos\left(\phi_i-\phi_n\right).$$

Inserting these equations, we perform exact numerical calculation of the FI. The results of the numerical calculation are plotted in Fig. 13, and we observe that with multipair correlations $\sigma_{\Delta\phi}\approx\sqrt{(3/N_q)}$. In summary, single-pair correlations cannot surpass the uncertainty of $1/\sqrt{2}$, while using all pair correlations a sensitivity of $\sqrt{3/N_q}$ is obtained, that is very close to the noiseless limit ($\sqrt{2/N_q}$).

3. Comparison with qubit-resolved readout

We can compare the performance of global readout described above with qubit-resolved readout. It is simple to see that given all N-qubit correlations the two methods perform the same. For qubit-resolved readout, the probability of an outcome vector $\mathbf{q}$ depends only on the total number of excitations in each ensemble:

$$p(\mathbf{q}|\varphi)=\frac{2^{-N_qN}}{2\pi}\cdot\int_0^{2\pi}d\varphi\prod_{j=1}^{N}\binom{N_q}{m_j}(1+\sin\left(\phi_j+\varphi\right))^{m_j} \times(1-\sin\left(\phi_j+\varphi\right))^{N_q-m_j},$$

where m_j is the total number of excitations in the jth ensemble: $m_j=\frac{1}{2}(\sum_i q_{j,i}+N_q)$. Therefore qubit-resolved readout does not add information.

On the other hand, if we are using only pair correlations in the postprocessing, qubit-resolved readout improves the precision for small N. In more detail, estimating the phase differences from all of the multipair correlations of qubits $\{\langle\sigma_{i,m}^x\sigma_{j,k}^x\rangle\}_{i,m,j,k}$ leads to better sensitivity for small N than using only the ensemble correlations $\{\langle Y_mY_k\rangle\}_{m,k}$. The calculation of the FI matrix with multipair correlations of qubits is the same as the multipair correlation calculation in Appendix A, just with different phases. Instead of N_qN different phases, we have N different phases such that ϕ_j is the phase of qubits $(j-1)N_q+1,\ldots,jN_q$. The FI matrix is then given by Eq. (A2), where Σ is the relevant $\binom{N_qN}{2}\times\binom{N_qN}{2}$ covariance matrix and D is the relevant $\binom{N_qN}{2}\times N$ derivative matrix. The results are shown in Fig. 13, where we observe that qubit-resolved readout can lead to a considerable improvement for $N\leq 3$, but already for $N=4$ the improvement is negligible. At the limit of large N, both the uncertainty with qubit-resolved readout and global readout converge to $\sqrt{3/N_q}$.

[1] A. D. Ludlow, M. M. Boyd, J. Ye, E. Peik, and P. O. Schmidt, *Optical atomic clocks*, Rev. Mod. Phys. **87**, 637 (2015).

[2] B. Canuel, F. Leduc, D. Holleville, A. Gauguet, J. Fils, A. Virdis, A. Clairon, N. Dimarcq, C. J. Bordé, A. Landragin, and P. Bouyer, *Six-axis inertial sensor using cold-atom interferometry*, Phys. Rev. Lett. **97**, 010402 (2006).

[3] A. Peters, K. Y. Chung, and S. Chu, *Measurement of gravitational acceleration by dropping atoms*, Nature (London) **400**, 849 (1999).

[4] P. Hamilton, M. Jaffe, P. Haslinger, Q. Simmons, H. Müller, and J. Khoury, *Atom-interferometry constraints on dark energy*, Science **349**, 849 (2015).

[5] R. Bouchendira, P. Cladé, S. Guellati-Khélifa, F. Nez, and F. Biraben, *New determination of the fine structure constant and test of the quantum electrodynamics*, Phys. Rev. Lett. **106**, 080801 (2011).

[6] V. Giovannetti, S. Lloyd, and L. Maccone, *Advances in quantum metrology*, Nat. Photonics **5**, 222 (2011).

[7] D. J. Wineland, J. J. Bollinger, W. M. Itano, F. L. Moore, and D. J. Heinzen, *Spin squeezing and reduced quantum noise in spectroscopy*, Phys. Rev. A **46**, R6797 (1992).

[8] J. J. Bollinger, W. M. Itano, D. J. Wineland, and D. J. Heinzen, *Optimal frequency measurements with maximally correlated states*, Phys. Rev. A **54**, R4649 (1996).

[9] C. D. Marciniak, T. Feldker, I. Pogorelov, R. Kaubruegger, D. V. Vasilyev, R. van Bijnen, P. Schindler, P. Zoller, R. Blatt, and T. Monz, *Optimal metrology with programmable quantum sensors*, Nature (London) **603**, 604 (2022).

[10] S. F. Huelga, C. Macchiavello, T. Pellizzari, A. K. Ekert, M. B. Plenio, and J. I. Cirac, *Improvement of frequency standards with quantum entanglement*, Phys. Rev. Lett. **79**, 3865 (1997).

[11] R. Demkowicz-Dobrzański, J. Kołodyński, and M. Guţă, *The elusive Heisenberg limit in quantum-enhanced metrology*, Nat. Commun. **3**, 1063 (2012).

[12] A. W. Chin, S. F. Huelga, and M. B. Plenio, *Quantum metrology in non-Markovian environments*, Phys. Rev. Lett. **109**, 233601 (2012).

[13] J. Jeske, J. H. Cole, and S. F. Huelga, *Quantum metrology subject to spatially correlated Markovian noise: Restoring the Heisenberg limit*, New J. Phys. **16**, 073039 (2014).

[14] D. Braun, G. Adesso, F. Benatti, R. Floreanini, U. Marzolino, M. W. Mitchell, and S. Pirandola, *Quantum-enhanced measurements without entanglement*, Rev. Mod. Phys. **90**, 035006 (2018).

[15] M. Chwalla, K. Kim, T. Monz, P. Schindler, M. Riebe, C. F. Roos, and R. Blatt, *Precision spectroscopy with two correlated atoms*, Appl. Phys. B **89**, 483 (2007).

[16] S. Olmschenk, K. C. Younge, D. L. Moehring, D. N. Matsukevich, P. Maunz, and C. Monroe, *Manipulation and detection of a trapped* Yb^+ *hyperfine qubit*, Phys. Rev. A **76**, 052314 (2007).

[17] K. Beloy and M. Bodine *et al.* [Boulder Atomic Clock Optical Network (BACON) Collaboration], *Frequency ratio measurements at 18-digit accuracy using an optical clock network*, Nature (London) **591**, 564 (2021).

[18] M. Takamoto, T. Takano, and H. Katori, *Frequency comparison of optical lattice clocks beyond the Dick limit*, Nat. Photonics **5**, 288 (2011).

[19] T. L. Nicholson, M. J. Martin, J. R. Williams, B. J. Bloom, M. Bishof, M. D. Swallows, S. L. Campbell, and J. Ye, *Comparison of two independent* Sr *optical clocks with* 1×10^{-17} *stability at* 10^3 **s**, Phys. Rev. Lett. **109**, 230801 (2012).

[20] B. P. Lanyon, P. Jurcevic, C. Hempel, M. Gessner, V. Vedral, R. Blatt, and C. F. Roos, *Experimental generation of quantum discord via noisy processes*, Phys. Rev. Lett. **111**, 100504 (2013).

[21] C. W. Chou, D. B. Hume, M. J. Thorpe, D. J. Wineland, and T. Rosenband, *Quantum coherence between two atoms beyond* $Q = 10^{15}$, Phys. Rev. Lett. **106**, 160801 (2011).

[22] G. E. Marti, R. B. Hutson, A. Goban, S. L. Campbell, N. Poli, and J. Ye, *Imaging optical frequencies with* 100 μHz *precision and* 1.1 μm *resolution*, Phys. Rev. Lett. **120**, 103201 (2018).

[23] R. Shaniv, N. Akerman, T. Manovitz, Y. Shapira, and R. Ozeri, *Quadrupole shift cancellation using dynamic decoupling*, Phys. Rev. Lett. **122**, 223204 (2019).

[24] E. R. Clements, M. E. Kim, K. Cui, A. M. Hankin, S. M. Brewer, J. Valencia, J.-S. Chen, C.-W. Chou, D. R. Leibrandt, and D. B. Hume, *Lifetime-limited interrogation of two independent* $^{27}Al^+$ *clocks using correlation spectroscopy*, Phys. Rev. Lett. **125**, 243602 (2020).

[25] A. W. Young, W. J. Eckner, W. R. Milner, D. Kedar, M. A. Norcia, E. Oelker, N. Schine, J. Ye, and A. M. Kaufman, *Half-minute-scale atomic coherence and high relative stability in a tweezer clock*, Nature (London) **588**, 408 (2020).

[26] C. F. Roos, M. Chwalla, K. Kim, M. Riebe, and R. Blatt, *'Designer atoms' for quantum metrology*, Nature (London) **443**, 316 (2006).

[27] E. Megidish, J. Broz, N. Greene, and H. Häffner, *Improved test of local Lorentz invariance from a deterministic preparation of entangled states*, Phys. Rev. Lett. **122**, 123605 (2019).

[28] T. Manovitz, R. Shaniv, Y. Shapira, R. Ozeri, and N. Akerman, *Precision measurement of atomic isotope shifts using a two-isotope entangled state*, Phys. Rev. Lett. **123**, 203001 (2019).

[29] T. Monz, P. Schindler, J. T. Barreiro, M. Chwalla, D. Nigg, W. A. Coish, M. Harlander, W. Hänsel, M. Hennrich, and R. Blatt, *14-qubit entanglement: creation and coherence*, Phys. Rev. Lett. **106**, 130506 (2011).

[30] C. E. Bradley, J. Randall, M. H. Abobeih, R. C. Berrevoets, M. J. Degen, M. A. Bakker, M. Markham, D. J. Twitchen, and T. H. Taminiau, *A ten-qubit solid-state spin register with quantum memory up to one minute*, Phys. Rev. X **9**, 031045 (2019).

[31] K. Singh, C. E. Bradley, S. Anand, V. Ramesh, R. White, and H. Bernien, *Mid-circuit correction of correlated phase errors using an array of spectator qubits*, Science **380**, 1265 (2023).

[32] B. Braverman, A. Kawasaki, and V. Vuletić, *Impact of non-unitary spin squeezing on atomic clock performance*, New J. Phys. **20**, 103019 (2018).

[33] B. C. Sawyer, J. W. Britton, A. C. Keith, C.-C. Joseph Wang, J. K. Freericks, H. Uys, M. J. Biercuk, and J. J. Bollinger, *Spectroscopy and thermometry of drumhead modes in a mesoscopic trapped-ion crystal using entanglement*, Phys. Rev. Lett. **108**, 213003 (2012).

[34] U. von Lüpke, F. Beaudoin, L. M. Norris, Y. Sung, R. Winik, J. Y. Qiu, M. Kjaergaard, D. Kim, J. Yoder, S. Gustavsson, L. Viola, and W. D. Oliver, *Two-qubit spectroscopy of spatiotemporally correlated quantum noise in superconducting qubits*, PRX Quantum **1**, 010305 (2020).

[35] S. Kawamura and Y. Chen, *Displacement-noise-free gravitational-wave detection*, Phys. Rev. Lett. **93**, 211103 (2004).

[36] Y. Chen, A. Pai, K. Somiya, S. Kawamura, S. Sato, K. Kokeyama, R. L. Ward, K. Goda, and E. E. Mikhailov, *Interferometers for displacement-noise-free gravitational-wave detection*, Phys. Rev. Lett. **97**, 151103 (2006).

[37] T. Gefen, R. Tarafder, R. X. Adhikari, and Y. Chen, *Quantum precision limits of displacement noise free interferometers*, Phys. Rev. Lett. **132**, 020801 (2024).

[38] K. Modi, A. Brodutch, H. Cable, T. Paterek, and V. Vedral, *The classical-quantum boundary for correlations: Discord and related measures*, Rev. Mod. Phys. **84**, 1655 (2012).

[39] T. J. Proctor, P. A. Knott, and J. A. Dunningham, *Multiparameter estimation in networked quantum sensors*, Phys. Rev. Lett. **120**, 080501 (2018).

[40] W. Ge, K. Jacobs, Z. Eldredge, A. V. Gorshkov, and M. Foss-Feig, *Distributed quantum metrology with linear networks and separable inputs*, Phys. Rev. Lett. **121**, 043604 (2018).

[41] Z. Eldredge, M. Foss-Feig, J. A. Gross, S. L. Rolston, and A. V. Gorshkov, *Optimal and secure measurement protocols for quantum sensor networks*, Phys. Rev. A **97**, 042337 (2018).

[42] J. Rubio, P. A. Knott, T. J. Proctor, and J. A. Dunningham, *Quantum sensing networks for the estimation of linear functions*, J. Phys. A **53**, 344001 (2020).

[43] D. Kiesenhofer, H. Hainzer, A. Zhdanov, P. C. Holz, M. Bock, T. Ollikainen, and C. F. Roos, *Controlling two-dimensional Coulomb crystals of more than 100 ions in a monolithic radio-frequency trap*, PRX Quantum **4**, 020317 (2023).

[44] M. K. Joshi, A. Fabre, C. Maier, T. Brydges, D. Kiesenhofer, H. Hainzer, R. Blatt, and C. F. Roos, *Polarization-gradient cooling of 1D and 2D ion Coulomb crystals*, New J. Phys. **22**, 103013 (2020).

[45] F. Kranzl, M. K. Joshi, C. Maier, T. Brydges, J. Franke, R. Blatt, and C. F. Roos, *Controlling long ion strings for quantum simulation and precision measurements*, Phys. Rev. A **105**, 052426 (2022).

[46] M. Schmidt, E. van den Berg, M. Friedlander, and K. Murphy, *Optimizing costly functions with simple constraints: A limited-memory projected quasi-newton algorithm*, in *Proceedings of the 12th International Conference on Artificial Intelligence and Statistics (AISTATS)* (Association for Computing Machinery, New York, 2009).

[47] W. H. Holtzman, *The unbiased estimate of the population variance and standard deviation*, Am. J. Psychol. **63**, 615 (1950).

[48] T. M. Cover, *Elements of Information Theory* (Wiley, New York, 1999).

[49] S. L. Braunstein and C. M. Caves, *Statistical distance and the geometry of quantum states*, Phys. Rev. Lett. **72**, 3439 (1994).

[50] J. Liu, H. Yuan, X.-M. Lu, and X. Wang, *Quantum Fisher information matrix and multiparameter estimation*, J. Phys. A **53**, 023001 (2019).

[51] T. Bothwell, C. J. Kennedy, A. Aeppli, D. Kedar, J. M. Robinson, E. Oelker, A. Staron, and J. Ye, *Resolving the gravitational redshift across a millimetre-scale atomic sample*, Nature (London) **602**, 420 (2022).

[52] X. Zheng, J. Dolde, V. Lochab, B. N. Merriman, H. Li, and S. Kolkowitz, *Differential clock comparisons with a multiplexed optical lattice clock*, Nature (London) **602**, 425 (2022).

[53] I. S. Madjarov, A. Cooper, A. L. Shaw, J. P. Covey, V. Schkolnik, T. H. Yoon, J. R. Williams, and M. Endres, *An atomic-array optical clock with single-atom readout*, Phys. Rev. X **9**, 041052 (2019).

[54] P. Kómár, E. M. Kessler, M. Bishof, L. Jiang, A. S. Sørensen, J. Ye, and M. D. Lukin, *A quantum network of clocks*, Nat. Phys. **10**, 582 (2014).

[55] B. C. Nichol, R. Srinivas, D. P. Nadlinger, P. Drmota, D. Main, G. Araneda, C. J. Ballance, and D. M. Lucas, *An elementary quantum network of entangled optical atomic clocks*, Nature (London) **609**, 689 (2022).

[56] D. H. E. Dubin, *Theory of structural phase transitions in a trapped Coulomb crystal*, Phys. Rev. Lett. **71**, 2753 (1993).

[57] J. Kiethe, L. Timm, H. Landa, D. Kalincev, G. Morigi, and T. E. Mehlstäubler, *Finite-temperature spectrum at the symmetry-breaking linear to zigzag transition*, Phys. Rev. B **103**, 104106 (2021).

[58] I. E. Linington and N. V. Vitanov, *Robust creation of arbitrary-sized Dicke states of trapped ions by global addressing*, Phys. Rev. A **77**, 010302(R) (2008).

[59] M. Um, J. Zhang, D. Lv, Y. Lu, S. An, J.-N. Zhang, H. Nha, M. S. Kim, and K. Kim, *Phonon arithmetic in a trapped ion system*, Nat. Commun. **7**, 11410 (2016).

[60] R. Lechner, C. Maier, C. Hempel, P. Jurcevic, B. P. Lanyon, T. Monz, M. Brownnutt, R. Blatt, and C. F. Roos, *Electromagnetically-induced-transparency ground-state cooling of long ion strings*, Phys. Rev. A **93**, 053401 (2016).

[61] X. Zheng, J. Dolde, M. C. Cambria, H. M. Lim, and S. Kolkowitz, *A lab-based test of the gravitational redshift with a miniature clock network*, arXiv:2207.07145.

[62] H. Hainzer, D. Kiesenhofer, T. Ollikainen, M. Bock, F. Kranzl, M. K. Joshi, G. Yoeli, R. Blatt, T. Gefen, and C. F. Roos, *Correlation spectroscopy with multiqubit-enhanced phase estimation: Data*, 10.5281/zenodo.6396594, 2022.

[63] S. M. Kay, *Fundamentals of Statistical Signal Processing: Estimation Theory* (Prentice-Hall, Englewood Cliffs, NJ, 1993).

[64] R. Demkowicz-Dobrzanski, U. Dorner, B. J. Smith, J. S. Lundeen, W. Wasilewski, K. Banaszek, and I. A. Walmsley, *Quantum phase estimation with lossy interferometers*, Phys. Rev. A **80**, 013825 (2009).

[65] L. Pezze, M. A. Ciampini, N. Spagnolo, P. C. Humphreys, A. Datta, I. A. Walmsley, M. Barbieri, F. Sciarrino, and A. Smerzi, *Optimal measurements for simultaneous quantum estimation of multiple phases*, Phys. Rev. Lett. **119**, 130504 (2017).